4

Data Analysis and Results

Online testing for the CE-06 experiment began in March, 1992, and continued through August of that year, at which point the detector setup and readout design methods were finalized. Production data were taken in December, 1992, and February, 1993, at proton energies of 166, 200, 250, 295, 330, and 350 MeV, using both fiber and foil carbon targets. This chapter discusses the analysis of this data along with the resulting cross-sections obtained near the single-pion reaction thresholds and in the region of possible double-pion production.

4.1 The Analysis Method: An Overview

The experiment described herein is primarily a study of two-body reactions in which the momentum of one emission product is much larger than that of the other. Positive pions produced via $^{12}\mathrm{C}(\mathrm{p},\pi^+)^{13}\mathrm{C}$, for example, have $\vec{p}_{\pi,\mathrm{lab}} \approx \vec{p}_{\pi,\mathrm{cms}}$ whereas the recoil ^{13}C ions' momenta satisfy $\vec{p}_{\mathrm{ion,lab}} \approx \vec{p}_{\mathrm{ion,cms}} + \vec{P}_{\mathrm{cms}}$. For $E_p = 166$ MeV, in particular, the ^{13}C ions have laboratory momenta comparable to the proton beam ($p \approx p_{\mathrm{beam}} \approx 580$ MeV/c) while the pions' momenta are smaller by an order of magnitude ($p_\pi \approx 60$ MeV/c). As seen in Fig. 2.7, this momentum mismatch results (in the laboratory frame) in a quasi-elliptical kinematic locus in the p-θ plane, with a well-defined maximum angle θ_{max} and two possible momenta values for each emission angle. The low- and high-momenta "branches" of the (p,θ) locus correspond to the forward ($0^\circ \leq \theta \leq 90^\circ$) and backward ($\theta > 90^\circ$) scattering of the light particle in the center-of-mass system (CMS), respectively (see Fig. 4.1). For

CMS pion distributions which are strongly forward-peaked, the projection of the p-θ ellipse onto the momentum axis results in a well-defined group in the momentum (and kinetic energy) distribution of the recoils. A localization of recoils in a high-energy group similarly corresponds to a backward-peaked pion distribution.

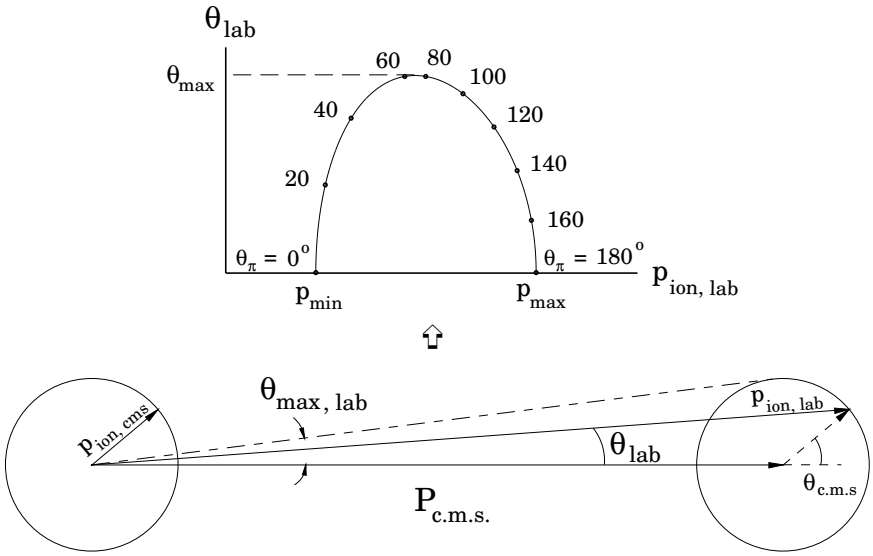

Figure 4.1 Center-of-mass and laboratory kinematics for two-body reactions such as $^{12}\mathrm{C}(\mathrm{p},\pi^+)^{13}\mathrm{C}$. For a given beam energy, there is only one degree-of-freedom in the system: $\theta_{\mathrm{cms}} = \theta_{\mathrm{cms}}(p,\theta)$. See also Fig. 2.7.

For a kinematically complete recoil measurement of reactions of this type, the data at each energy should provide: a) identification of the reaction particles, and b) the recoil momentum and emission angle in the laboratory system. Requirement (a) can be met, if the process is a two-body reaction, by determining the mass M and atomic number Z of the ion.[1] The measurement of (b) then allows the determination of the system's single degree of freedom, the center-of-mass angle θ_{cms}, and the cross-section follows.

Figure 4.2 graphically shows the raw data variables that are measured by the CE-06 detector apparatus, along with the desired intermediate[2] and final[3] calculated quantities that are necessary to determine in order to satisfy conditions (a) and (b). The raw data includes two-dimensional measurements of the intercepts of the ion track at the PGAC and PC-Si active areas which, given the physical location of each detector in magnet

[1] For three-body final states with a p + ^{12}C entrance channel, this is true only for certain limiting cases, for example, $M = 13$ amu.

[2] Half-baked.

[3] Cooked.

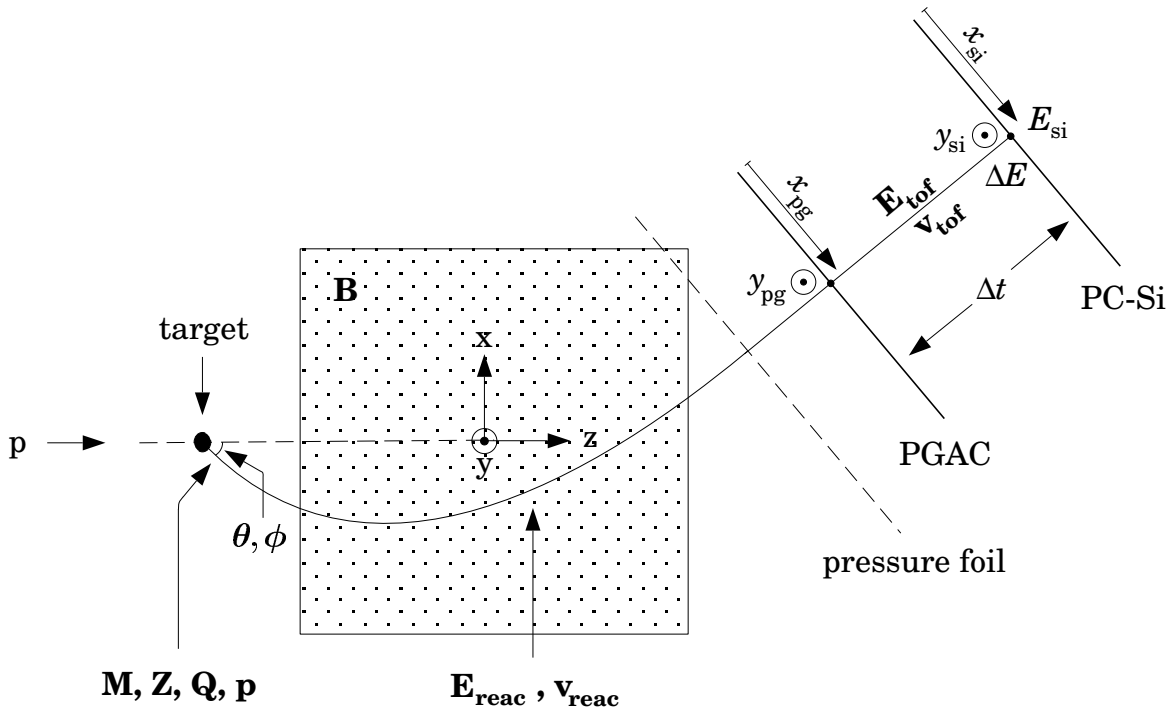

Figure 4.2 The raw and calculated data involved in the CE-06 data analysis, for a single recoil ion flight path. Raw (directly measured) data are shown in italic, and calculated quantities are shown in bold. Figure is not drawn to scale.

coordinates (cf. App. C), yield the (x, y, z) location of the ion at two times in its flight path. With this information, the velocity of the ion while between the PGAC and PC can be calculated using the raw timing signals from the PGAC and Si detectors: $\Delta t = t_p - t_s$. The transmission energy loss ΔE in the PC active volume and the ion energy at the silicon array plane $E_{\rm si}$ complete the raw data obtained for each event.

Further analysis can take one of two paths, depending in effect on whether a complete ion identification can be made by the detector stack or not. In principle (i.e., without regard to detector resolutions), the analysis can proceed as follows. First, the ion nuclear charge is identified via the PC and silicon array detector measurements of ΔE and $E_{\rm si}$ along with Eq. (3.8). Next, the ion mass identification is made using the approximation

$$E_{\rm tof} = E_{\rm si} + k\,\Delta E \tag{4.1}$$

along with

$$M = 2 \cdot E_{\rm tof} \cdot \left(\frac{\Delta t}{l}\right)^2, \tag{4.2}$$

where k is a constant and l is the measured time-of-flight distance.[4]

[4] All of the ion identification calculations done here are non-relativistic: typically, $v_{\rm ion} \approx 0.05 \cdot c$.

Raytracing simulations, as described in App. C, can be used to determine the appropriateness of Eq. (4.1). Fig. 4.3 describes the predicted "true" relationship between $E_{\rm tof}$ and $E_{\rm si}$ as indicated by the solid curve, which can be well reconstructed by Eq. (4.1) with $k = 4.5$, independent of M and Z (since ΔE already contains the dependence on these variables). This value of k (the best fit of the simulated data to the solid curve of Fig. 4.3) is essentially the expected ratio of the total energy loss of the ion in the PC gas and foils to that lost in the active volume alone (ΔE). The mass determination tends to be least accurate for low ion energies (see Sec. 4.3.2).

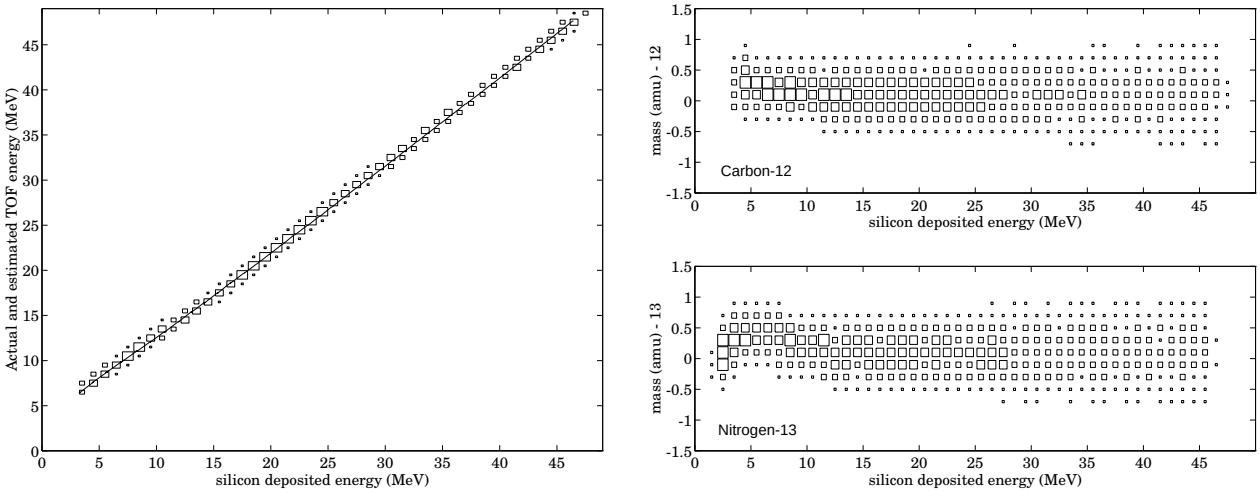

Figure 4.3 Simulated data using forward raytracing and the operating parameters (PC gas pressure, e.g.) from the production runs. At left is a comparison for ^{12}C between the "actual" (solid curve) and simulated $E_{\rm tof}$ values, the latter from Eq. (4.1) with $k = 4.5$. At right are the resulting reconstructed mass values M from Eq. (4.2) for ^{12}C and ^{13}N.

With the mass identification, the ion's flight path from the target can be determined by reconstruction of the ion's energy within the magnet ($E_{\rm reac}$, as in Fig. 4.2) using a method similar to Eq. (4.1) and then by raytracing backwards through the (known) magnetic field. Although the atomic charge Q is undetermined at this stage, the well-defined target location easily eliminates the incorrect charge state since each successively higher level of ionization is bent additionally by approximately six degrees. Given the proper charge Q, then, the ion is traced back to the target location, and the reaction parameters (p, θ, ϕ) are determined.

The uncertainties in Δt and $E_{\rm tof}$, primarily through the timing and PC resolutions, make the calculation of M via Eq. (4.2) inconclusive, however. In order to distinguish

between $M = 12$ and $M = 13$ ions[5], for example, a mass resolution of $\Delta M/M < 8\%$ (or 4% FWHM) is needed. With a timing resolution of 1.3 nsec FWHM, and Si and PC resolutions of approximately 150 keV and 60 keV, respectively, the mass resolution is roughly 5% FWHM, and so the masses are not fully resolved. The methods used to overcome this problem are detailed in Sec. 4.3. The general technique is as follows: first, a second calculation of $E_{\rm tof}$ is obtained using

$$E_{\rm tof} = b \cdot E_{\rm si} + a, \tag{4.3}$$

for constants a and b, which corresponds to fitting the solid curve of Fig. 4.3 to a straight line. This method has the advantage over Eq. (4.1) in that only the comparatively high-resolution Si energy measurement is used instead of the PC measurement. The constants a and b are dependent on the nuclear charge Z of the ion, however.

In analogy to Fig. 4.3, a simulation of the mass calculation via Eq. (4.3) is shown in Fig. 4.4, for ^{12}C and ^{13}N ions. The $E_{\rm tof}$ curves can be fit to straight lines with a maximum absolute error in $E_{\rm tof}$ of 400 keV for any value of $E_{\rm si}$. Restricting the range of silicon deposited energy values to $E_{\rm si} > 15$ MeV reduces the error to less than 175 keV; hence, the curves deviate from straight lines primarily for low ion energies. This deviation is reflected in the corresponding calculated mass values, shown in the figure for ^{12}C and ^{13}N, in which the variation from a "flat" mass locus occurs mainly for low-energy nitrogen ions. Although the mass loci obtained via Eq. (4.1) tend to be more well-behaved for very low ion energies[6], the benefit in the use of Eq. (4.3) lies in the small width of the low-energy mass contours of Fig. 4.4 compared to Fig. 4.3.

Using the measured ion track positions, the backward raytracing methods of App. C are then applied to yield the rigidity and projected angle of the ion at the target. Coupled with the velocity measurement, the ratio M/Q can be determined. A reasonable determination of both M and Q can be made by studying the M (from (4.2) and (4.3)) vs. M/Q correlation. With the rigidity and angle data, the calculation of the ion's reaction parameters is complete. Before any part of this procedure can be applied to the raw data obtained in the experiment, however, it is necessary to calibrate accurately all of the CE-06 detectors; this is the subject of the next section.

---

[5] Masses will be specified implicitly in atomic mass units for the remainder of this work.

[6] The mass calculation method using Eq. (4.1) does not require the $E_{\rm tof}$ curves to be linear in $E_{\rm si}$.

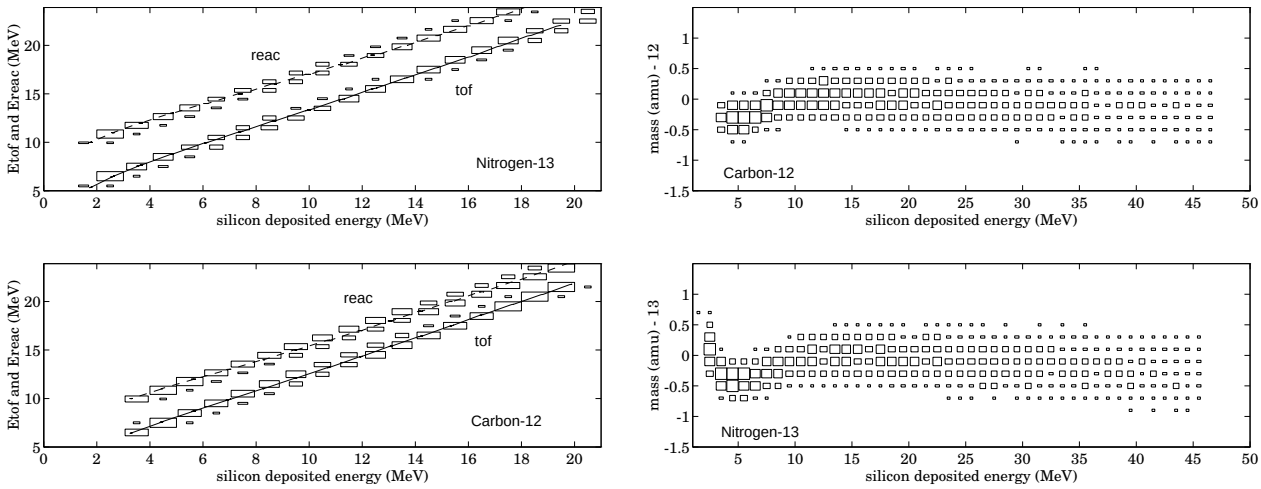

Figure 4.4 Simulated mass reconstructions (right) using only the Si energy measurement. The solid curves at left are the "actual" $E_{\rm tof}$ values for ^{12}C and ^{13}N, superimposed over simulated $E_{\rm tof}$ data using reasonable detector resolutions and Eq. (4.3). Also shown are the corresponding $E_{\rm reac}$ curves (dashed lines) and reconstructions from Eq. (4.6).

4.2 Calibration of the Detector Stack

The calibration of the detectors for CE-06 is a non-trivial but necessary prelude to the data analysis. The procedure is made complicated mainly by two factors: a) the multi-element array nature of the detectors (specifically, the Si and PC components) necessitates the gain (and offset) alignment of many channels; b) the relative insensitivity of some components (e.g., the PGAC) to standard radioactive sources (of γ rays or α particles) implies that some of the calibrations must be done internally, i.e., using the online data. There are four primary aspects of the calibration procedure, involving the silicon energy $E_{\rm si}$, the PC transmission energy loss ΔE, the Si and PGAC $\vec{x}$ measurements, and the PGAC-Si timing.

4.2.1 Silicon Energy Measurement

The matching of the twenty-four Si energy signal channels is the most straightforward element in the calibration process. The desired goal is to match the gains and offsets of all the energy signal channels; these two parameters are matched roughly in the hardware and then fine-tuned in the analysis software. A proper calibration is achieved when the summed resolution is comparable to that of an average single detector.

The multi-line α sources ^{228}Th and ^{226}Ra each provide at least four strong, well-defined energy calibration lines between roughly 4 and 8 MeV. For the CE-06 production runs, a collimated source was placed on an externally adjustable rod located directly in

front of the PC pressure foil. This source could illuminate each of the twelve columns of detector pairs (cf. Fig. 3.31) separately, with minimal interference of intervening material. As such, the proper correspondence of hardware and software channels was checked and the intrinsic resolutions of individual detectors were measured. For 8 MeV α particles, energy resolutions across the array ranged from 130 to 170 keV.

For efficient and time-effective gain matching of all the detectors, however, it was necessary to illuminate many or all of the detectors at once. A slightly collimated source (about 2 mm in width) was placed directly on the target ladder for this purpose, with an aluminum plate mounted to the side of the beam to block α particles from entering the detector stack while a target was in use. This arrangement had several advantages: a) the entire array of 24 silicon detectors could be illuminated by the source, with an appropriate choice of the 6° magnet current; b) the source could be inserted or retracted remotely via the external target ladder controls, independent of ring access, during production runs; and c) the rough operation of the remaining detectors (PC and PGAC) could be checked.

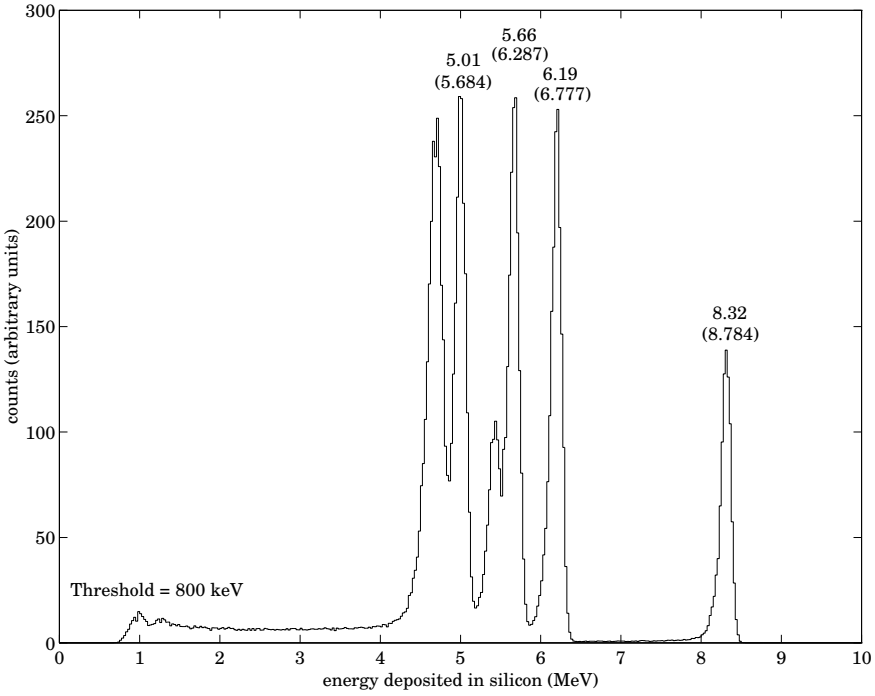

Figure 4.5 Summed energy spectrum of the silicon array illuminated with a ^{228}Th α source. Shown are the deposited energies in MeV corresponding to the source energies in parentheses. The other lines were not used in the calibration. Energy straggling is negligible here compared to the detector resolutions.

Figure 4.5 shows the calibrated Si energy signal, summed (logically) over the array,

with a ^{228}Th target source. The calibration source line centroids in the individual Si chip spectra were fitted to straight lines, whose gains and offsets were then adjusted via software corrections to convenient values. A drawback of the use of the target-mounted source for Si energy calibration is the energy losses of the α particles in the intervening foils. The losses range from approximately 500 to 700 keV, or roughly 10% of the emission energies. Forward raytracing was therefore implemented to provide the abscissas for the straight line fits, which improved the fit quality (maximum deviations from a straight line were roughly 20 keV) compared to fits using the source energies. The centroid locations of the rod source α lines agreed with this calculation within the overall Si energy resolution of about 150 keV.

4.2.2 The PC Calibration

The PC is comprised of twenty-five independent sense wires, each with separate readout electronics. The next step in the calibration process is the gain matching of these signals, which in principle is essentially identical to the procedure outlined in Sec. 4.2.1: a multi-line α source can be used to illuminate the wires, and with this data the overall gain variations among the wires can be determined. This calibration of the PC wires was, however, made significantly more difficult due to the small signals produced by the α source and to variations in single-wire gains along the length of the active area.

The small signals are a by-product of the thin active volume of the PC (see Fig. 3.14) and the relatively low ionization power of the α particles from the source. At typical operating gas pressures ($P \approx 25$ torr) for the production runs, the four α lines used for the Si energy calibration result in deposited energies in the PC active volume from 50 keV ($E_\alpha = 8.8$ MeV) to 75 keV ($E_\alpha = 5.7$ MeV). The difference of 25 keV across the source spectrum is comparable to the PC energy resolution, and so centroid measurements are difficult. The need to apply this calibration to PC signals representing deposited energies larger than this by a factor of 10 to 20 (see Fig. 4.3) further makes the α source of limited use.

Also complicating the calibration procedure was the variation in gain along the length of each sense wire. As detailed in Ch. 3, the cathode planes of the PC were constructed from wire grids to avoid the use of aluminized mylar foils. With approximately 700 wires per cathode plane, it was necessary to use tension of roughly 15 grams (a minimal amount) for each wire so as not to stress the (thin) aluminum frame. The electrostatic attraction of the cathode grid toward the anode along with the mechanical stresses in the frame

applied during the PC assembly procedure produced enough force to displace some of the cathode wires out of the plane, resulting in a position-dependent gain. For this PC design ($C_{\text{wire}} \approx 7$ pF/m), a variation in the cathode-to-anode distance of 0.3 mm is enough to produce a 25% variation in gain for an event occurring in that region (see App. A). Figure 4.6 shows typical results for several representative wires: the gain variation is maximal (at roughly 25%) for wires near the physical center of the active area (located in magnet coordinates at $y \approx 0.4$ cm). Here, the cathode wire deflection is greatest, since the grids are attached to the PC frame at the top and bottom of the active area.

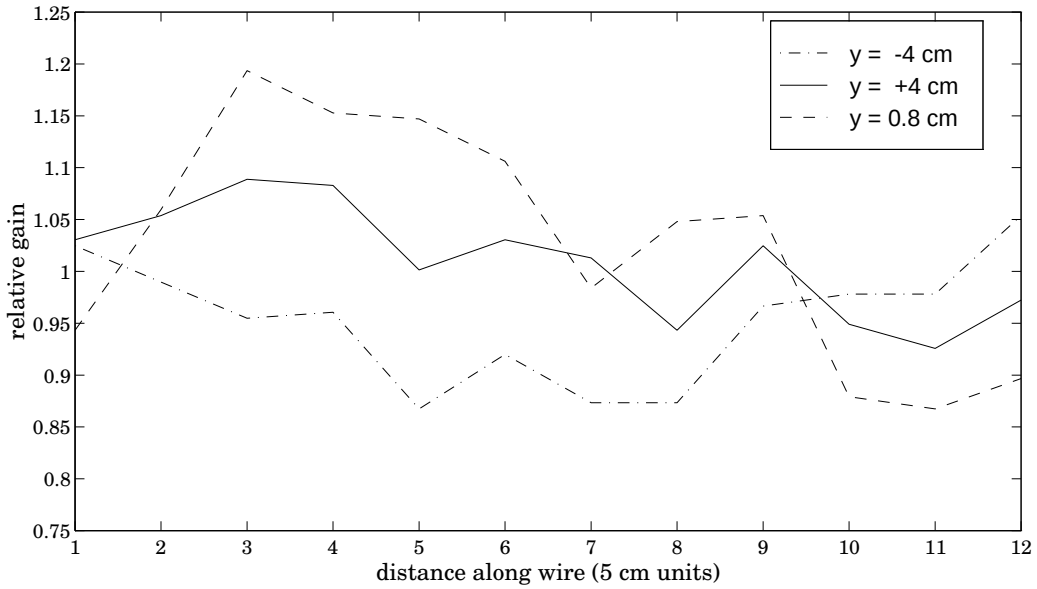

Figure 4.6 Characteristic gain variations in the PC wires, measured using the online α spallation recoils at $E_\alpha \approx 2.5$ MeV. Shown are gains (averaged over 5 cm lengths of wire) relative to the overall average.

These two main problems, the inapplicability of the target-mounted α source, and the x_{si}-dependent PC wire gain variations, were solved to a fair degree of success. Essentially, the calibration was carried out by using the internal ($3 \leq Z \leq 6$) data for gain matching with signal sizes in the region of interest, coupled with the Si energy and position measurements. The method is as follows: first, a narrow region of particle energies is chosen via a window on the Si linear signals. The window is made as narrow as possible, typically about 1 MeV in width, without sacrificing reliable PC centroid measurements. The PC signals that satisfy this gate are then plotted, for each wire, as a function of Si position, and centroid measurements are taken for a reasonable[7] x_{si} gate width. From this data, a

[7] As with the silicon energy, "reasonable" means as small as possible given the total number of counts.

table of multiplicative correction constants is generated, which allows the gain matching to be performed in the analysis software. For the production runs, a gate width of 4 mm was used, resulting in more than 3800 PC calibration constants.

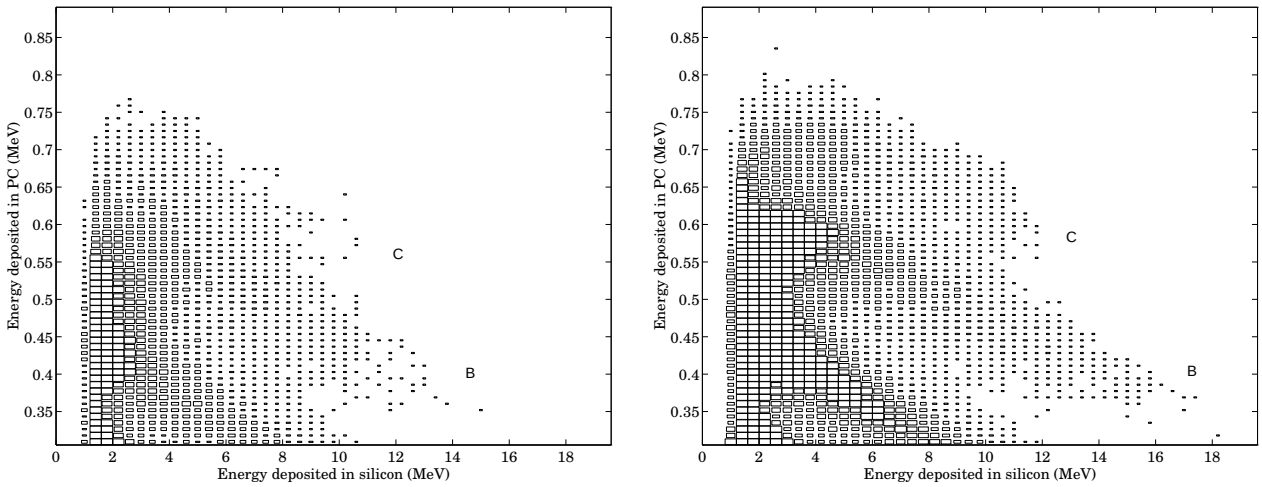

Figure 4.7 The boron and carbon region of the particle ID spectrum (ΔE vs $E_{\rm si}$) with (right) and without (left) the correction for gain variation along the wires. See also Fig. 4.11. The count density scales are the same for both figures.

A representative comparison of data with and without the calibration is shown in Fig. 4.7, where the improvement in the particle ID Z-separation is seen to be quite significant (cf. Sec. 4.3.1). Most of the overall gain fluctuation from wire to wire is due to the mechanical problems mentioned above, with less than 10% of the total variation from differences in pre-amp and ADC channel gains. As mentioned in Ch. 3, the PC was operated during the production runs at a reduced bias voltage to decrease the gain factor m, since the relative change in gain $\Delta m/m$, due to mechanical variations, depends approximately linearly on the applied voltage (cf. App. A).

4.2.3 The PGAC and Si Position Calibration

The next part of the process, the position calibration, is necessary to provide the connection between the raw position data and the corresponding magnet coordinates of the ion track's interception with the PGAC and Si detectors. In particular, the goal of the position calibration is the determination of (using the notation of Fig. 4.2) the transformations

$$\begin{aligned} (x_{\rm pg}, y_{\rm pg}) &\longmapsto (x, y, z)_{\substack{\rm PGAC, \\ \rm magnet}}, \\ (x_{\rm si}, y_{\rm si}) &\longmapsto (x, y, z)_{\substack{\rm Si, \\ \rm magnet}}. \end{aligned} \tag{4.4}$$

Since the T-Site magnet is primarily a dipole with $\mathbf{B} \approx -B\hat{y}$, and the detector active areas are oriented parallel to the y-axis, (4.4) is comprised of two decoupled transformations: one for the (x, z) coordinates and the other for the out-of-plane y positions. With these functions, the methods of App. C can be applied to determine the rigidity (R) and angles (θ and ϕ) of the ion at the reaction point.

In order to develop the coordinate transformation for the CE-06 data, it was necessary to know: a) the location of the active areas of the detectors with respect to an external reference mark on their housings, and b) the position of these marks in magnet coordinates. To determine the latter, the detectors were placed in position before the first production run (and left unmoved until the end of the second run), and direct measurements of the reference mark positions were made relative to the magnet fiducial pins (see Fig. C.2).[8] Two reference marks per detector were necessary for a complete, three-dimensional position measurement. The desired (and achieved) precision for these measurements was 1–2 mm; the knowledge of the absolute position of the ion at this level is necessary to achieve a 1–2% measurement of the ion rigidity.

Direct measurements on the detector housings were then made in order to accomplish (a). For the PC-Si detector, this was relatively straightforward; for the PGAC dimensions, however, only estimates could be made, particularly for the size of the gap between the two electrically distinct halves of the active area. The inductive position readout of the PGAC, as opposed to the discrete nature of the PC and Si detectors (and consequent correspondence of position to physical elements such as wires or strips), requires indirect measurements of its active area to be made using source data.

The procedure for these measurements is as follows: first, data is taken with a target-mounted α source (which is in a known position). Next, the direct measurements are incorporated as external parameter constants in the forward raytracing, along with the best estimates of the parameters that could not be determined directly, such as the PGAC gap. Simulated α particle data is produced with the raytracing (using the location of the α source) and compared to the real data, from which appropriate adjustments are made to the data-analysis position parameters[9], the raytracing constants, or both.

Adjustment of the parameters is accomplished by studying the relationship of the

---

[8] In reality, for reasons of physical accessibility, the relative positions (to the fiducial pins) of three monuments were first determined, and *these* were used as reference points.

[9] These constants are gain and offset parameters which convert the raw position data to the magnet coordinate system.

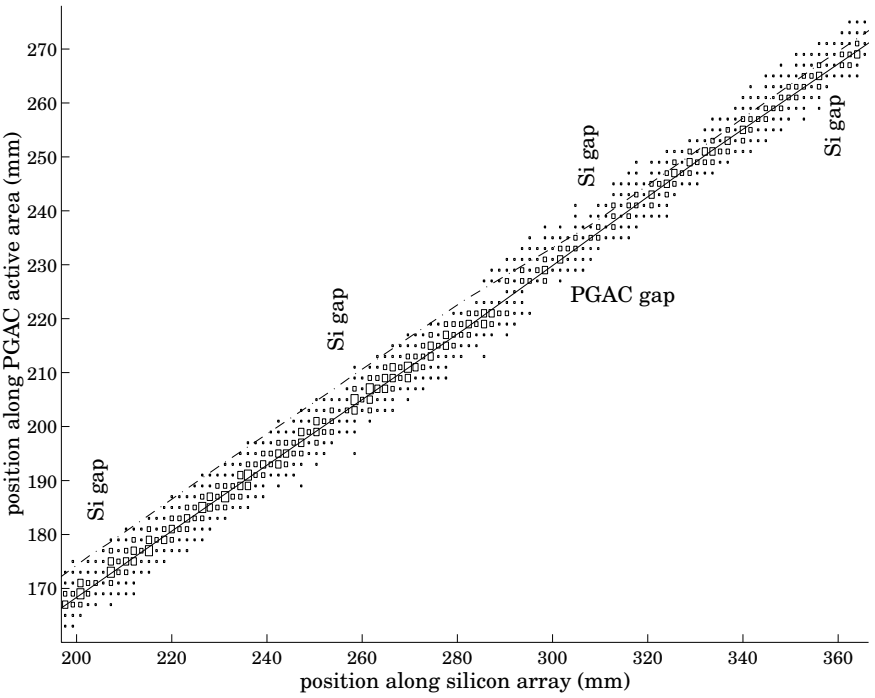

Figure 4.8 The measured position data $x_{\rm pg}$ vs. $x_{\rm si}$, using 6.777 MeV α particles and the final position parameter values, near the middle of the active area of the PGAC. The solid line is the expected relationship from forward raytracing. The dashed line is a fit to the original ("uncorrected") data. The 1.3 mm gaps between silicon detectors (at roughly every 50 mm) and the 3 mm pgac gap (near $x_{\rm pg} = 225$ mm) are also visible.

PGAC position measurement $x_{\rm pg}$ to the Si measurement $x_{\rm si}$, which is predicted to be a straight line by the simulations. The slope of the line is primarily sensitive to the angle of the detectors' active areas (in the x-z plane), whereas the offset depends mainly on the location of the beam-side edges of these areas. Although the true slope is determined fairly accurately using the direct position measurement data, the offset value cannot be determined in this way due to the uncertainties in the location of the PGAC $x_{\rm pg}$-plane edges. The needed adjustments in the position parameters should therefore involve significant corrections only to the offset value.

Figure 4.8 shows representative data (real and simulated) from which these adjustments were made. As expected, the slopes of the fitted data line and simulation line matched within the error of the simulation (this error stems primarily from uncertainties in the direct measurements), and only minor changes to the offsets, due mostly to the gap between halves of the PGAC, were necessary. As seen in the figure, the apparent width[10]

[10] This width is, in large part, due to the fact that the α source was not finely collimated.

of the measured data locus is comparable to the needed offset adjustments of roughly 3 mm. The data and simulated lines were therefore considered to be in agreement when the rigidity value for the α particle (obtained via the methods of App. C) was independent of $x_{\rm pg}$, within the rigidity resolution. This comparison further allowed an second check of the absolute rigidity value calculation; in the case of Fig. 4.8, the measured α rigidity value of $112.8 \pm .4$ MeV/c agrees well with the tabulated value of $p/Q = 112.5$ MeV/c.

A similar linear relationship exists between the out-of-plane position measurements $y_{\rm pg}$ and $y_{\rm si}$ from the PGAC and PC, respectively (the vertical position measured at the PC is virtually identical to the (unmeasured) y position at the silicon). In this case, however, the direct measurements were sufficiently accurate that no adjustments in the vertical position parameters were necessary. In part, this was due to the fact that $y_{\rm pg}$ plane of the PGAC is a single unit, unlike the $x_{\rm pg}$ plane, and the vertical locations of the detector housings were easily measured with a precision of 0.5 mm or better.

At this point, the transformation of raw position data to magnet coordinates is implicitly defined in the forward raytracing (and similarly in the backward code) and the position calibration is complete. The absolute uncertainties in the position measurements resulting from this calibration (including detector resolutions) are on the order of 3 mm, corresponding to absolute errors in rigidity and bend-plane angle of 1–2% and 0.1°, respectively. These values represent the combined intrinsic resolution of the magnet and detector stack (with this particular analysis method) as a "spectrograph." The effective vertical position resolution of 4 mm (dominated by the position resolution of the PC) corresponds to an intrinsic, vertical angular resolution of roughly 0.4°.

4.2.4 The Absolute Timing Calibration

The final step in the calibration procedure is the gain and offset matching of the twenty-four timing channels (one for each silicon detector), in order that the time-of-flight between the PGAC and Si for any event can be determined. Although an *absolute* calibration is not necessary in this case, since the velocity is mainly useful in the construction of a scaled (and discrete) quantity such as the ion's mass M, the complete determination of Δt is a natural consequence of the calibration method detailed below.

The timing calibration is similar in method to that used for the Si energy, although the disadvantages of the low ionization power of the α source as described in Sec. 4.2.2 apply here also. In this case, the PGAC, which provides the timing start signal, is relatively insensitive to the α particles, so that the anode signal is small and fails to provide optimum

timing (the resolution figure quoted in Sec. 3.4.2 was obtained using sulfur ions). The data for the timing calibration were therefore taken using the $Z = 4$ spallation products (^{7}Be and ^{9}Be, mainly) as a compromise between available counts and reliable performance of the PGAC.

The timing data for $Z = 4$ were measured in five narrow slices of $E_{\rm si}$, with typical full widths of roughly 0.4 MeV, and ranging in value from 7 to 16 MeV; the corresponding time-of-flight values ranged from 32 to 53 nsec. Using simulation data for the abscissa values, straight line fits were made to the data from each silicon detector. From these, twenty-four gain and offset pairs were constructed to provide the connection $t_{\rm raw} \mapsto t_{\rm tof}$. This procedure matches gains and offsets while providing an absolute calibration.

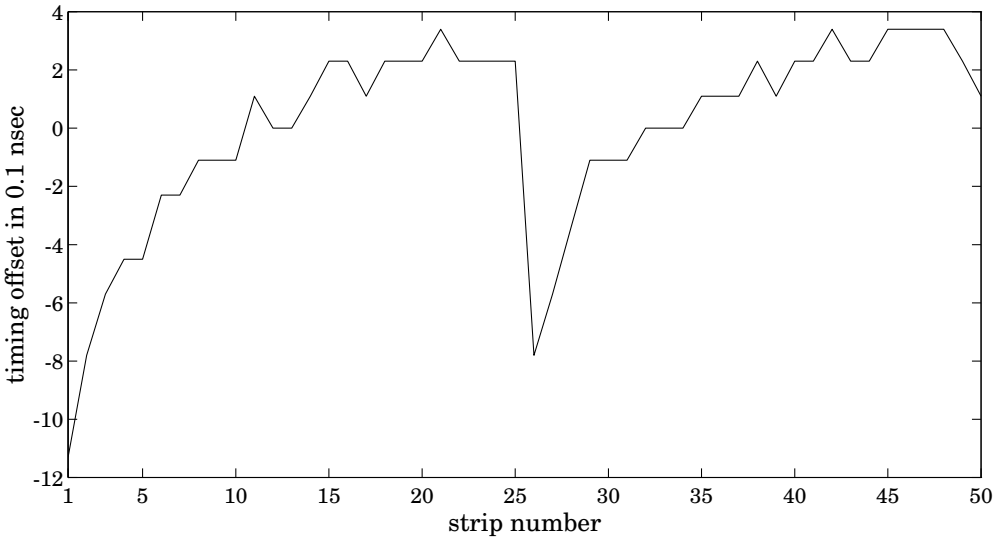

Figure 4.9 Timing offsets, in 0.1 nsec units, for each strip on a CE-06 Si chip, due to the variation in signal-wire lengths on the attached PCB. The maximum deviation from the average is 1.1 nsec.

A complication in the timing procedure arises due to the variations in signal-wire lengths on the circuit boards directly attached to the Si wafers (see Fig. 3.20). This introduces a position-dependence of the timing that cannot be corrected by a single gain/offset pair per chip. Since this is an effect of the Si chip alone, however, it is a straightforward procedure to measure these timing differences from strip to strip using the α source.

Typical data for a single chip is shown in Fig. 4.9. The circuit board is essentially divided into two blocks of 25 signal wires each, producing the large change in offset at the middle of the Si wafer. Since the circuit boards for all of the Si chips are identical, a table of 50 timing offsets suffices to provide the appropriate corrections. In this way, an overall

time-of-flight resolution of 1.3–1.4 nsec was achieved.

4.3 First-Level Analysis: Z, M, Q, p/Q, and θ

E_p (MeV)	ν_p (MHz)	C target	t ("data on")	t (elapsed)
$165.4 \pm .05$	1.81902	foil	3 hr. 18 min.	7 hr. 52 min.
$165.5 \pm .05$	1.81934	fiber	7 hr. 04 min.	18 hr. 12 min.
$199.0 \pm .06$	1.95236	fiber	9 hr. 35 min.	19 hr. 58 min.
$248.9 \pm .08$	2.11660	fiber	8 hr. 41 min.	16 hr. 05 min.
$293.7 \pm .10$	2.23877	foil	9 hr. 45 min.	15 hr. 10 min.
$328.5 \pm .12$	2.32100	foil	6 hr. 12 min.	9 hr. 59 min.
$330.4 \pm .12$	2.32527	both	29 hr. 19 min.	45 hr. 24 min.
$348.3 \pm .13$	2.36368	fiber	11 hr. 51 min.	28 hr. 48 min.

Table 4.1 CE-06 data summary. Beam frequencies refer to $N = 1$ synchotron mode. Events were recorded only during the "data on" time. The foil target was 6.2 μg/cm^2 thick, and the fiber was 4.2 μg/cm^2 thick by 8.3 μm wide. Both fiber (67% of the time) and foil (32%) targets were used at $E_p = 330$ MeV.

A summary of the CE-06 production run data is shown in Table 4.1. The difference between the "data-on" and elapsed times represents the time lost to Cooler ring overhead (filling, ramping, etc.). As discussed in Ch. 3, the listed uncertainties in the unpolarized proton beam energies are primarily systematic.

The essential goal of the first level of analysis of this data is the complete identification of the recoil ions (M, Z, and Q) along with the determination of their reaction parameters (p, θ, and ϕ). Although several different calibrations were used in the analysis (since the data were taken in two runs and three different gain settings for the Si pre-amps were used), the steps in this part of the analysis are the same for all the data. This section describes the identification procedure in detail.

4.3.1 Atomic Number (Z)

The first (and, in principle, the most straightforward) step in the identification process is the determination of the atomic number Z. With the α-particle data as a calibration for $Z = 2$, the PC and Si measurements ΔE and $E_{\rm si}$ can be used, coupled with Eq. (3.8), to separate the different species of ions. The use of the PC measurement ΔE here requires, however, that the (unknown) total ion energy *before* entrance into the PC active volume be

used in the equation, not $E_{\rm si}$. Nonetheless, for most ion types and energies typical to the CE-06 experiment (see Table C.1), this differentiation is minor and does not significantly affect the ability to resolve Z.

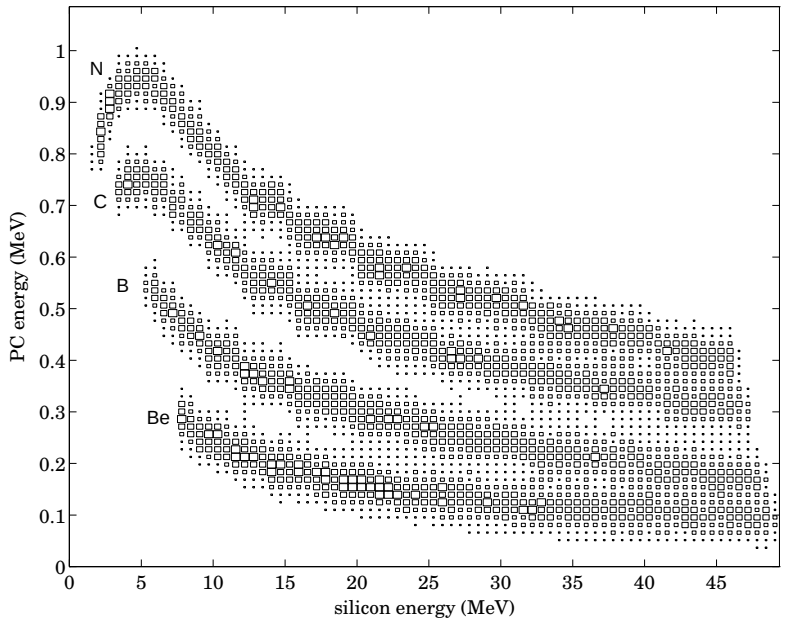

Figure 4.10 A simulation of ΔE (PC) vs. $E_{\rm si}$, using a CF_4 pressure of 22 torr, with characteristic detector resolutions included. The incident ions range in (reaction emission) energy from 10 to 50 MeV.

Figure 4.10 shows simulation data that tends to confirm this hypothesis: For all but very low-energy nitrogen ions ($E_{\rm si} \lesssim 2$ MeV), the product $\Delta E \cdot E_{\rm si}$ easily separates different values of Z (although different masses are *not* resolved). The curves for carbon and nitrogen ions turn over below deposited energies in the silicon of approximately 4 and 5 MeV, respectively. In this region, the specific energy loss of Eq. (3.7) begins to decrease as the ion velocity increases, and Z separation becomes difficult.

Particle identification data taken at $E_p = 166$ MeV is shown in Fig. 4.11. The extremely intense locus[11] for $Z = 2$ has been removed in the figure to clarify the heavier ion groups. The separation between groups is fairly clear except for the low-energy recoils with $Z \geq 5$. In order to properly define a Z-gate (such as that shown for carbon in Fig. 4.12), conditions are placed on the particle ID spectrum to clarify the location of the different groups for low energies. The basic procedure is as follows: first, a rough Z-gate is drawn in the particle ID. Next, using the mass calculation methods of Sec. 4.3.2 (which require

[11] Low-energy spallation α particles were by far the most abundant background in the CE-06 experiment.

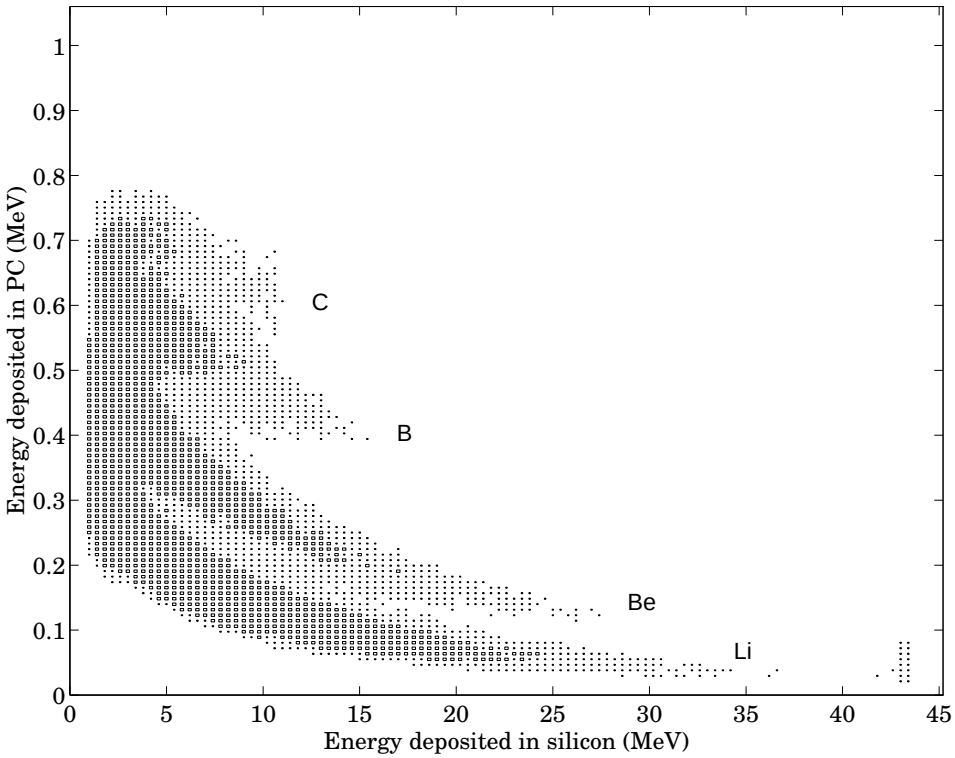

Figure 4.11 The "particle ID" spectrum, ΔE vs. $E_{\rm si}$, for the $E_p = 166$ MeV data. The clipping limits for the PC and Si measurements are roughly 1 MeV and 42 MeV, respectively. The count density scale is logarithmic.

at least a rough knowledge of Z, see below), a characteristic mass condition is specified for the ID, and the Z-gate is redrawn. This procedure is implemented by beginning with $Z = 4$ and working up to the nitrogen group.

A spectrum from this procedure, used for a more precise determination of the $Z = 6$ gate, is shown in Fig. 4.12. Here, an $M = 13$ condition clarifies the upper edge of the $Z = 6$ group, the knowledge of which is important for separation of the $Z = 6$ and $Z = 7$ loci. Similarly, the lower edge of the $Z = 6$ gate is determined previously, by construction of the $Z = 5$ gate, using a characteristic (i.e., commonly produced) mass for boron, such as $M = 10$. Mass values $M = 7$ and $M = 9$ are strongly produced in beryllium spallation products (there are, however, no expected characteristic nitrogen isotopes).

4.3.2 Nuclear Mass (M) and Atomic Charge (Q)

The next step in the analysis is the determination of the ion mass M and atomic charge Q. Although the pair (Z, M) uniquely identifies the recoil, it is further necessary to measure Q to allow calculation of the momentum p using the rigidity (see Sec. 4.3.3). The primary goal of this part of the analysis is to identify charge states from $Q = 3$ to

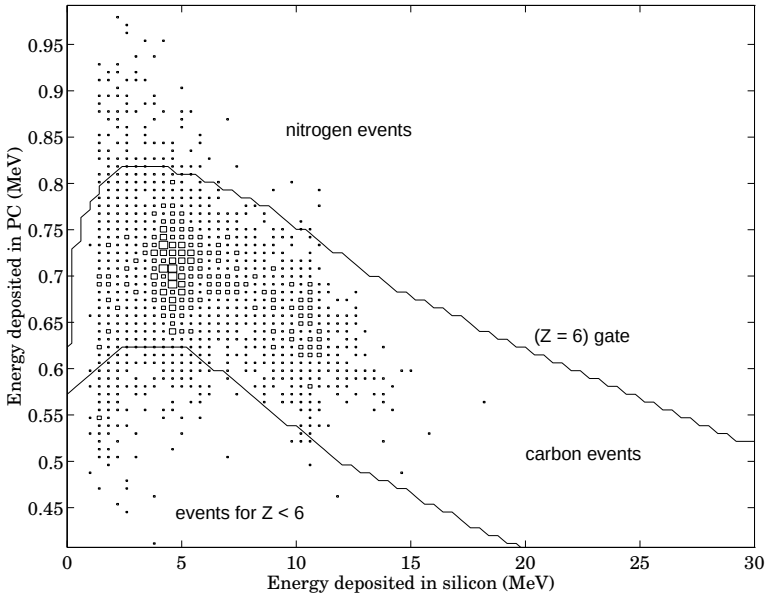

Figure 4.12 Upper portion of the particle ID spectrum, for events satisfying the PC mass condition $M = 13$ (cf. Sec. 4.3.2). The two groups inside the gate at $E_{\rm si}$ values of roughly 5 and 10 MeV are events corresponding to $^{12}\mathrm{C}(\mathrm{p},\pi^+)^{13}\mathrm{C}$. Also shown is the final gate for $Z = 6$.

$Q = 7$ and to distinguish between $M = 12$ and $M = 13$ ions, since the latter are indicative of events corresponding to reactions of interest in this work, and the former are a common background.

There are three primary techniques to calculate ion masses from the CE-06 data. The first and most intuitive of these incorporates the PC measurement ΔE along with relations (4.1) and (4.2). The application of this method to data for $E_p = 166$ MeV is shown in Fig. 4.13. In general, the value of k is adjusted until the mass contours are independent of the silicon energy $E_{\rm si}$, i.e., "flat" as in the figure. This is necessary in order to minimize the width of the projected mass locus and to separate the loci at low energies ($E_{\rm si} \lesssim 5$ MeV).

The resolution of the PC data is, however, not sufficient for complete separation of the $M = 12$ and $M = 13$ ions. The identification is acceptable for desired mass separation at the 22% level (as in the case of beryllium) but not as low as 8% (as needed for carbon). Nonetheless, once the value of k is determined for any value of Z (such as for Be ions), Eq. (4.1) is valid for all ion species, and this mass determination is useful for fine adjustment of other gates (as seen previously in Sec. 4.3.1). The parameter value used in the analysis ($k = 4.7$) compares favorably to the raytracing value ($k = 4.5$) given the expected 15% uncertainty of the energy-loss tables. For the analysis of the CE-06 data, the PC mass

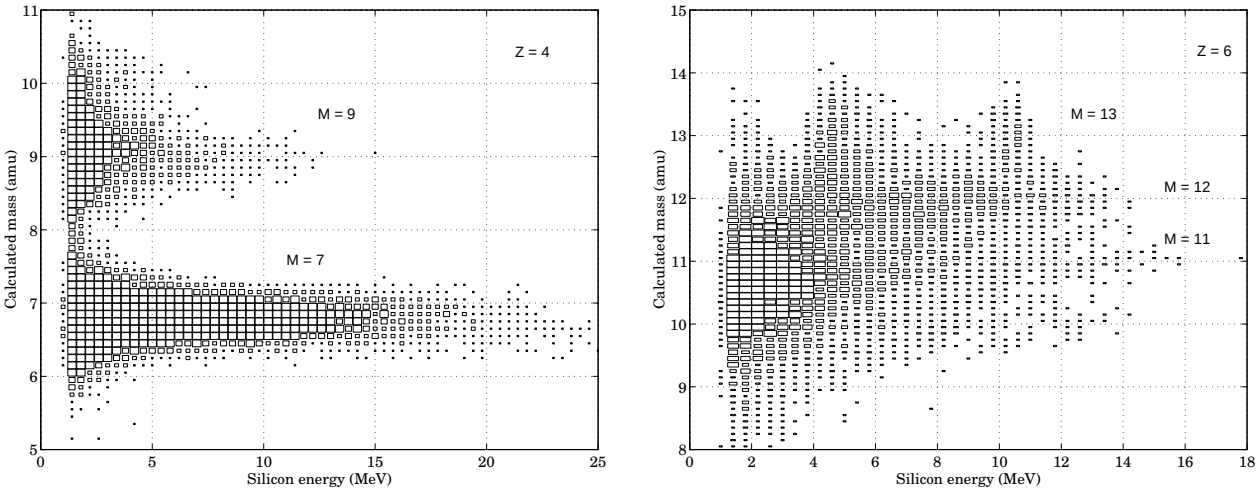

Figure 4.13 Mass determination using the PC for $Z = 4$ (left) and $Z = 6$ (right). The strong groups shown consist of ^{7,9}Be and ^{11,12,13}C. The well-known strong production of the Be isotopes allows the overall scaling of this "PC mass" quantity, along with the determination of the (Z-independent) value of k.

calculation was primarily used to ensure the proper gating and scaling of the more precise but Z-dependent means of mass determination detailed below.

The second method of mass calculation uses only the silicon measurement $E_{\rm si}$, coupled with Eqs. (4.3) and (4.2), in order to avoid the use of the comparatively low-resolution ΔE measurement. As was seen in Fig. 4.4, the applicability of approximation (4.3) is reasonable down to silicon energy values near the maximum of the Bragg curve[12] at $E_{\rm si} \approx 4$ MeV. The parameters a and b are different for each ion species, however, as seen in Table 4.2, so that the analysis requires the determination of new values for each Z value.

Ion	$E_{\rm tof}$				$E_{\rm reac}$			
	b (MeV/MeV)		a (keV)		c (MeV/MeV)		d (keV)	
	data	sim	data	simulation	data	sim	data	simulation
Be	0.96	0.97	2150	1300 ± 50	0.93	0.94	3500	2800 ± 100
B	0.90	0.95	3000	2400 ± 100	0.87	0.90	5500	4800 ± 150
C	0.88	0.93	3800	3300 ± 100	0.85	0.86	7200	6900 ± 150
N	0.85	0.92	4400	4100 ± 150	0.83	0.84	8500	8700 ± 200

Table 4.2 Energy calculation parameters for the mass determination using Eqs. (4.3) and (4.6). Shown are the final data parameters used in the analysis and those expected from simulations.

[12] The curves in Fig. 4.10 are *not* Bragg curves, but the maxima are similar.

Using the raytracing simulations to generate first-order estimates, a method similar to that for the first mass calculation is employed to determine a and b: the parameters are varied until the mass contours M vs. $E_{\rm si}$ are independent of $E_{\rm si}$. The PC mass gate is used as a condition for the contour spectrum to simplify the two-dimensional search.[13] Except for the most heavily ionizing particles (such as nitrogen ions, for the CE-06 experiment), the "true" parameters do not differ greatly from those expected from simulations (see Table 4.2 and Fig. 4.4). In general, the linear fit (4.3) tends to underpredict M at low energies and overpredict at high values of $E_{\rm si}$. To compensate for this in the analysis, the final slope and offset parameters are somewhat lower and higher than the simulation parameters, respectively. This compensation tends to improve the mass calculation for $E_{\rm si} \lesssim 10$ MeV at the expense of minor underprediction for $E_{\rm si} \gtrsim 25$ MeV.

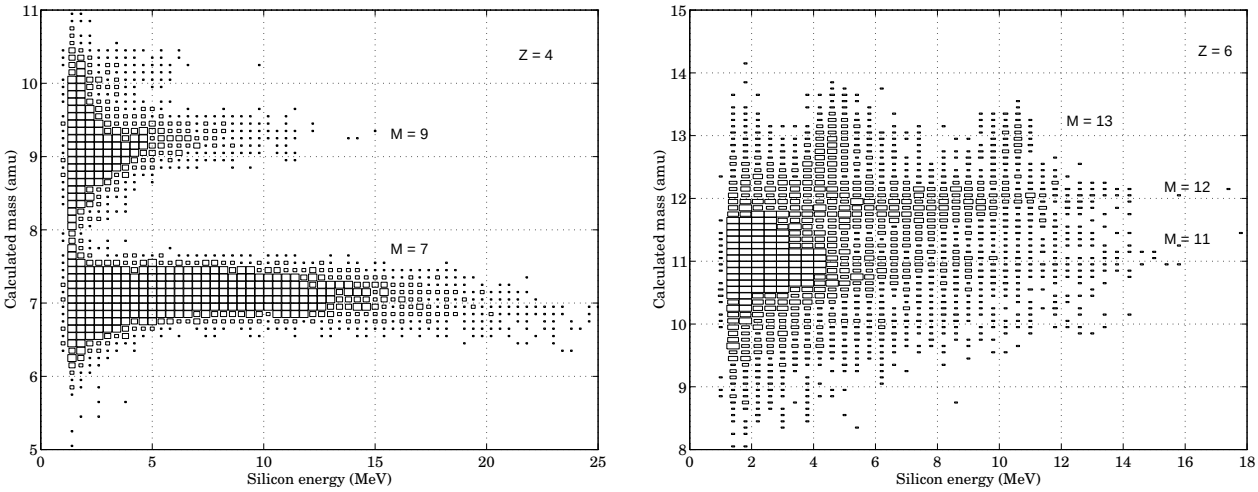

Figure 4.14 Mass determination using $E_{\rm si}$ (the "Si mass" method). Data shown is for $Z = 4$ and $Z = 6$ at $E_p = 166$ MeV (compare Fig. 4.13). The two groups at $M = 13$ correspond to $^{12}\mathrm{C}(\mathrm{p},\pi^+)^{13}\mathrm{C}$ (see also Fig. 4.12).

The application of this method to the carbon group for the $E_p = 166$ MeV data is shown in Fig. 4.14, where the improvement in resolution compared to the PC mass calculation is apparent (note especially the width of the locus for $M = 12$). The $M = 12$ and $M = 13$ groups at low energies are still not fully resolved, however. The mass separation is important in this regime ($E_{\rm si} \lesssim 5$ MeV): For the single-pion production reactions, the low-momentum branches of the kinematic loci (see Fig. 2.7) produce deposited energies in the silicon of a few MeV. The low-energy groups formed by the momentum projection

[13] Unlike k, parameters a and b implicitly define the mass scaling via (4.3) and (4.2); this scaling of the Si mass calculation is greatly simplified by pre-determination of M via the PC mass gate.

of these branches occur even for beam energies well above the thresholds of the reactions, since the low-momentum part of the loci do not "move" considerably over the energy range 166 MeV $< E_p <$ 350 MeV.

A third independent method of mass calculation is necessary to overcome the inability of either the first or second method to resolve $M = 13$ from $M = 12$. With the measurement of the ion's rigidity $R \equiv p/Q$, the mass can also be obtained via

$$M = \frac{RQ}{v_{\mathrm{reac}}}, \tag{4.5}$$

where v_{reac} is the ion velocity while inside the T-Site magnet chamber. The atomic charge Q can be determined in the following way: first, the energy of the ion during traversal of the magnet chamber, E_{reac}, is approximated (see Fig. 4.4) by

$$E_{\mathrm{reac}} = c \cdot E_{\mathrm{si}} + d, \tag{4.6}$$

where c and d are constants determined from raytracing simulations and the related parameters[14] in Eq. (4.3). Then, the atomic charge can be written as

$$Q \propto \frac{\sqrt{E_{\mathrm{tof}} E_{\mathrm{reac}}}}{v_{\mathrm{tof}} \cdot R}. \tag{4.7}$$

The characteristic charge-state populations measured via (4.7) for carbon at $E_p =$ 166 MeV are shown in Figure 4.15. Similarly to the silicon method of mass calculation, the Q contours are adjusted using c and d to be independent of the silicon energy, although the different charge states are well resolved even in the low-energy regime. Furthermore, since Q is quantized, an exact value can be used in Eq. (4.5) with no error contribution. The widths of the projections of the Q-contours are therefore irrelevant, assuming that a two-dimensional separation in the Q-E_{si} plane is possible.

The ion's velocity inside the magnet, v_{reac}, is calculated by applying a "velocity correction" to v_{tof}, which accounts for the energy loss suffered by the ion in the PGAC and in the magnet pressure foil. Since E_{reac} has already been estimated using Eq. (4.6), the correction is facilitated via

$$E'_{\mathrm{reac}} = c' \cdot (\frac{1}{2} m_0 v_{\mathrm{tof}}^2) + d', \tag{4.8}$$

[14] The "true" parameters for E_{tof} provide a guide for variations of the values from that expected from simulations.

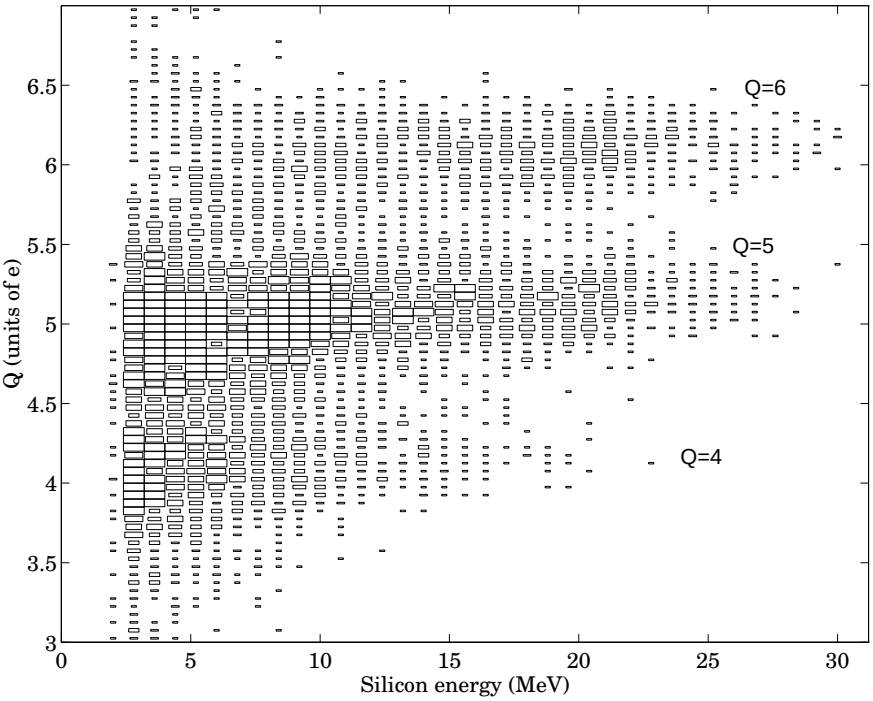

Figure 4.15 Atomic charge calculation, using (4.7) and the parameters of Table 4.2, applied to $Z = 6$ data at $E_p = 166$ MeV. Shown are the $Q = 4, 5, 6$ states of carbon.

and

$$v_{\text{reac}} = \sqrt{\frac{2E'_{\text{reac}}}{m_0}}, \tag{4.9}$$

where c' and d' are similar to but not the same as the parameters in (4.6). Here, m_0 is a provisional (exact) mass chosen to be close in value to the desired mass groups. As usual, c' and d' can be chosen by requiring the independence of the resulting mass (4.5) with respect to E_{si}.

Calculation of the mass via Eq. (4.5) is advantageous in that the relatively low-resolution timing measurement enters linearly through Eq. (4.9) rather than quadratically as in Eq. (4.2). However, the uncertainty in estimating the reaction energy[15] along with the use of another calculated quantity, R, yields a mass measurement comparable in quality to that obtained via the second method of calculation. Hence, neither of these mass calculations is alone able to provide a means of separating $M = 12$ and $M = 13$ ions. Final determination of the mass in the CE-06 data analysis was made by considering the *correlation* of the two results.

Figure 4.16 represents the combination of the second and third mass calculations via

[15] E_{reac} can be quite different from E_{si}, as shown in Table C.1.

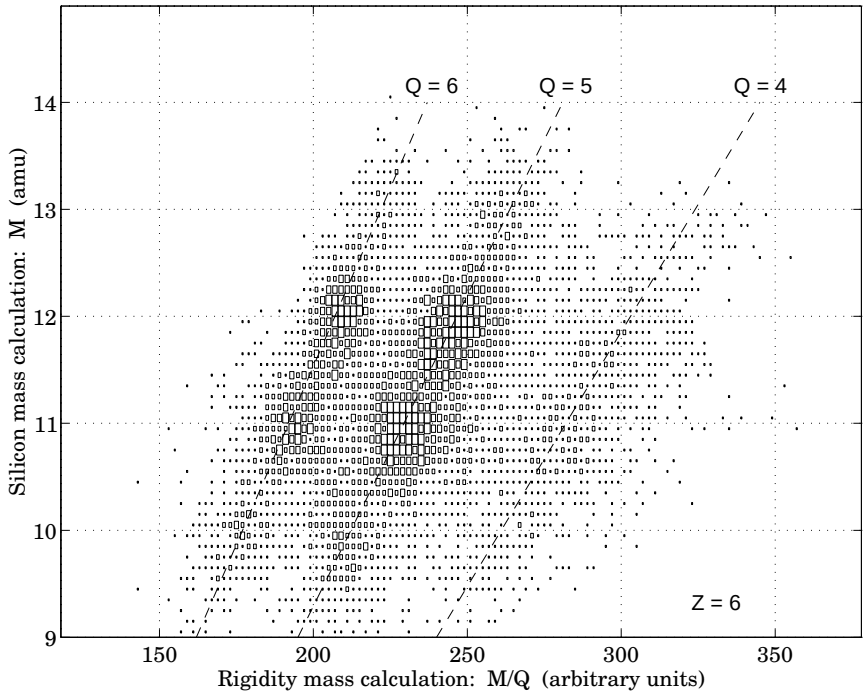

Figure 4.16 The mass and charge identification spectrum, for $Z = 6$ data at $E_p = 166$ MeV. Plotted are $M/Q = R/v_{\mathrm{reac}}$ horizontally and M (from (4.3) and (4.2)) vertically. Lines of constant mass and charge are horizontal and diagonal, respectively.

Eqs. (4.3) and (4.5), respectively. A mass and charge combination is selected using an appropriate two-dimensional gate on the spectrum. In this way, both measurements of the mass, each of which is not of sufficient resolution for separation of $M = 12$ and $M = 13$, are effectively combined to produce a satisfactory identification. Although the projections of these two mass groups onto either of the axes are not separable, the loci can be resolved sufficiently in the two-dimensional plane. The determination of Q is only necessary here to ensure proper charge calibration of the resulting M-Q gate. With knowledge of Z, the quantized mass value M completes the identification of the recoil ion.

4.3.3 Reaction Parameters: Momentum (p) and Angle (θ, ϕ)

The first level of analysis concludes with the determination of the recoils' reaction parameters (p, θ, ϕ) at the target. The rigidity R is obtained directly from the backward raytracing methods of App. C (and in fact this quantity was already used in the mass determination). Using the quantized value of the atomic charge Q, the ion emission momentum is obtained trivially via

$$p = RQ. \tag{4.10}$$

The backward raytracing also yields the ion's projected reaction angles in the x-z plane. Fig. 4.17 shows the geometrical relationship of the directly measured angular quantities θ_p and ϕ_s to the desired spherical angles θ and ϕ. The angle ϕ_s, defined in terms of the ion velocity components by $\tan\phi_s = v_y/\sqrt{v^2 - v_y^2}$, remains constant over the flight path[16], hence it is naturally measured by the detector stack using

$$\tan\phi_s = \frac{\Delta y}{\sqrt{(\Delta x)^2 + (\Delta z)^2}}, \tag{4.11}$$

where $\Delta(x, y, z)$ is the change in magnet coordinates of the ion track from the PGAC to the PC-Si intercepts.

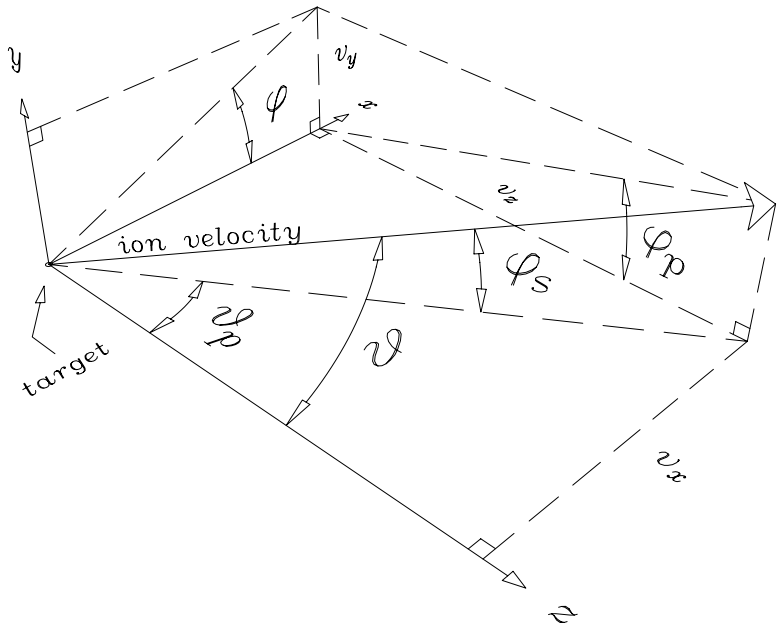

Figure 4.17 Definition of the measured and calculated angular quantities for the ion at the reaction point.

Assuming that $-90° < \theta_p < 90°$ (the T-Site horizontal plane acceptance is roughly $|\theta_p| < 25°$), the direction angle in the y-z plane is given by

$$\tan\phi_p = \frac{\tan\phi_s}{\cos\theta_p}, \tag{4.12}$$

which leads to determination of the spherical angle θ using

$$\tan^2\theta = \tan^2\phi_p + \tan^2\theta_p. \tag{4.13}$$

[16] This is actually a 1st-order approximation, due to the 6° magnet fringe field, but the 2nd-order corrections are much smaller than the detector stack's y resolution.

As a by-product, the azimuthal angle ϕ is then

$$\tan\phi = \frac{\tan\phi_p}{\tan\theta_p}, \tag{4.14}$$

the knowledge of which completes the determination of the recoil ions' kinematic parameters in the laboratory frame.

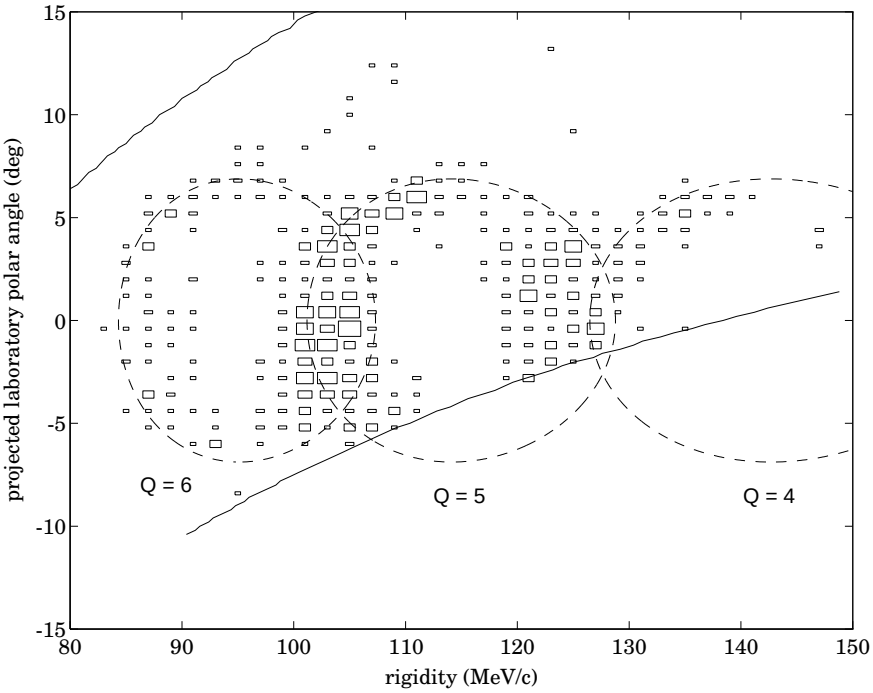

Figure 4.18 The R-θ_p relationship for ^{13}C events at $E_p = 166$ MeV. Also shown are the kinematics for $^{12}\mathrm{C}(\mathrm{p},\pi^+)^{13}\mathrm{C}_{\mathrm{g.s.}}$ (dashed lines) and the calculated acceptance (solid lines), both for $\phi_p = 0$).

The R-θ_p correlations for ^{13}C ions detected during the production runs at $E_p = 166$ MeV and $E_p = 294$ MeV are shown in Figures 4.18 and 4.19, respectively. The identification of ^{13}C implies that these events correspond uniquely to π^+ production from $^{12}\mathrm{C}(\mathrm{p},\pi^+)^{13}\mathrm{C}$, via conservation of baryon number and charge. At 166 MeV, the recoils are sufficiently confined in angle that the acceptance for $^{13}\mathrm{C}^{6+}$ ions is 4π steradians. In general, the projected kinematic ellipses may overlap for different charge states; however, these are separable since the atomic charge is known from the analysis of Sec. 4.3.2. The kinematics of $^{12}\mathrm{C}(\mathrm{p},\pi^+)^{13}\mathrm{C}_{\mathrm{g.s.}}$ are also shown in the figures, along with the calculated acceptances from the forward raytracing simulations. Many of the events occur on the inside edge of the expected ground-state ellipse; this suggests that there is a strong population of the bound

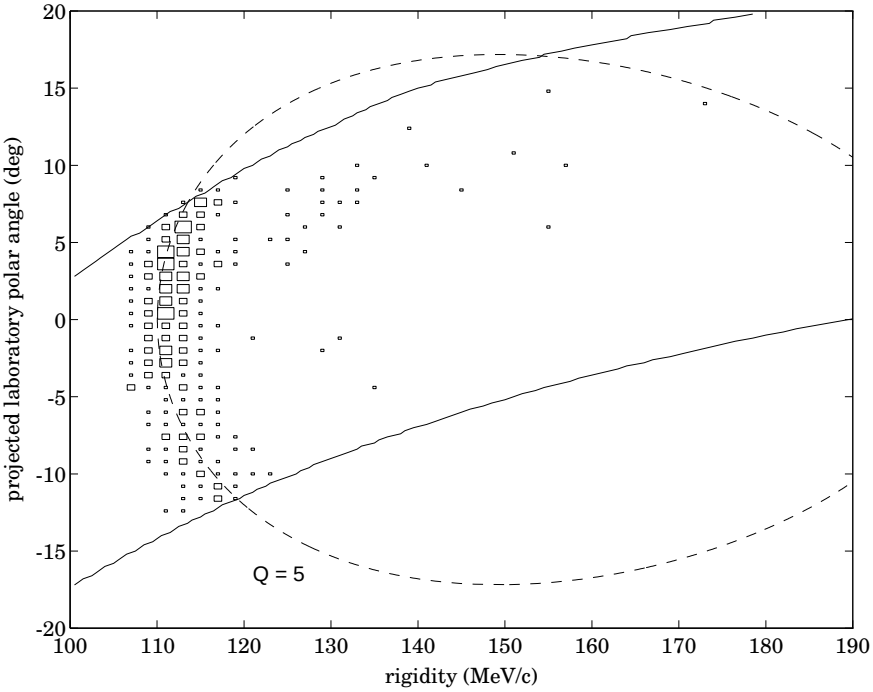

Figure 4.19 The R-θ_p relationship for $^{13}C^{5+}$ events at $E_p = 294$ MeV, with kinematics and acceptances shown for $\phi_p = 0°$ as in Fig. 4.18.

^{13}C excited states at 3.09, 3.68, and 3.85 MeV (this effect is not apparent in Fig. 4.19 due to the scale of the kinematic ellipse at $E_p = 294$ MeV).

Expressions (4.10), (4.13), and (4.14) lead to the end results—the kinematic ellipse of the recoils in the p-θ plane—of the first-level analysis. The events corresponding to (p, π^+) at $E_p = 166$ MeV are shown in Fig. 4.20, in which ions are observed along the entire locus of possible p-θ pairs. The projection in θ of this data is shown in Fig. 4.21, which tends to confirm the weakness of the ^{13}C ground-state contribution to the (p, π^+) reaction, since the maximum angle is sensitive[17] to the available kinematic energy. In principle, the beam energy E_p could be determined from $\theta_{\max}$ to a precision of roughly 500 keV; however, multiple scattering (see Sec. 4.4) artificially degrades the angular resolution and precludes this measurement. Also shown in the figure for completeness is the corresponding ϕ distribution, although this information is not needed in the analysis of the CE-06 data. The localization of counts near $\phi = 0°$, 180°, and 360° reflects the fact that the physical laboratory acceptance is primarily in the x-z plane.

The width of the kinematic overlay in Fig. 4.20 is zero since there is only one degree of freedom for the two-body reaction $^{12}\mathrm{C}(\mathrm{p}, \pi^+)^{13}\mathrm{C}$. A finite width in the data is expected

[17] At $E_p = 166$ MeV, $\theta_{\max}$ increases by 0.2° for every 1 MeV increase in E_p.

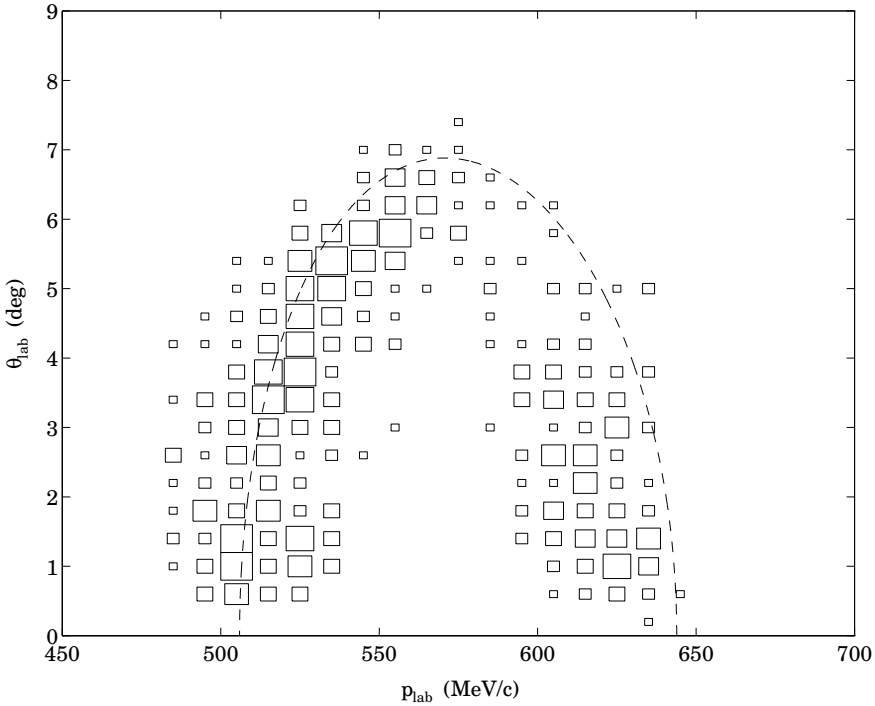

Figure 4.20 Kinematic locus for ^{13}C recoils at $E_p = 166$ MeV, using all detected charge states ($Q = 4, 5, 6$). The expected p-θ relationship for $^{13}\mathrm{C}_{\mathrm{g.s.}}$ ions from (p, π^+) is also shown (dashed line).

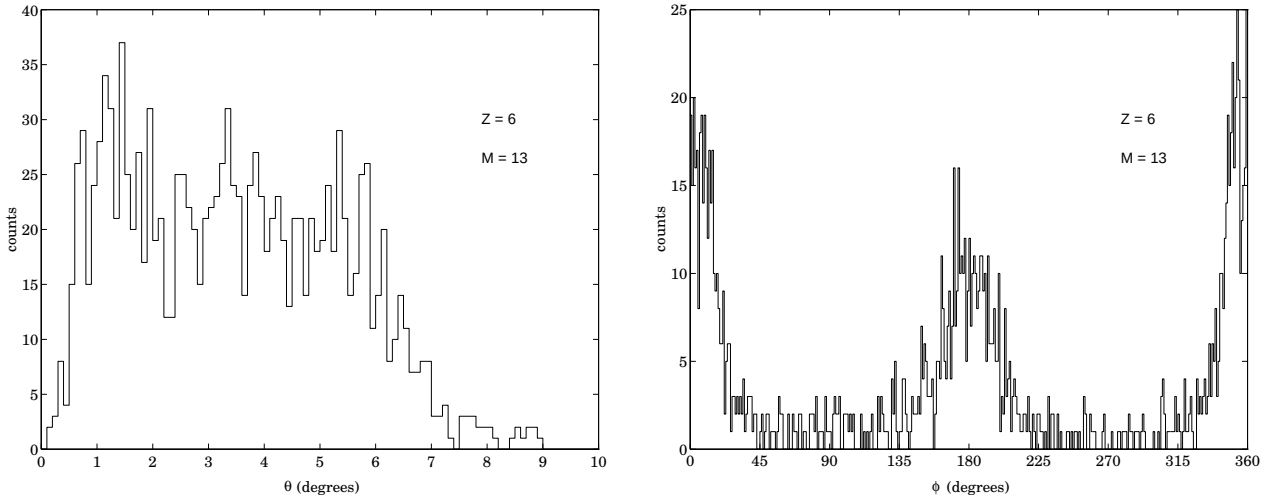

Figure 4.21 The θ (left) and ϕ (right) distributions for the ^{13}C events of Fig. 4.20. The expected maximum polar angles for the ground state and the 3.85 MeV excited state at $E_p = 166$ MeV are 6.75° and 5.82°, respectively.

due to the non-zero resolutions of the detector measurements; however, the width of the data locus in the figure is unexplained from the magnitude of the measured resolutions by roughly a factor of 2. Furthermore, the count distributions along the R-θ_p loci (see $Q = 5$

and $Q = 6$ at 166 MeV in Fig. 4.18, for example) are not symmetric about $\theta_p = 0$. The perceived asymmetry is unrealistic since the unpolarized beam and spinless target define no preferred direction in space. A misalignment of the beam direction from the magnet coordinate system z axis (see App. C) could produce such an asymmetry; however, the effect would simply be to shift the entire locus in a direction parallel to the θ_p axis of Fig. 4.18. This count distribution puzzle is a consideration for the next level of data analysis.

4.4 Second-Level Analysis: L_{int} and $d\sigma/d\Omega$

Given the unambiguous identification of the reaction process, and the laboratory p-θ distribution of the recoil ions (as in Fig. 4.20, for example), the corresponding differential cross-sections in the CMS can be obtained. In principle, this second stage of analysis can be accomplished analytically, as long as the charge-state populations (see Fig. 3.10), detector stack acceptances as a function of recoil rigidity and angle, and luminosities are known. For this work, however, variations in the measured p-θ ellipses due to multiple scattering of the ions, and difficulties in determining the true average luminosities, necessitated the use of numerical methods for calculation of $d\sigma/d\Omega$. This section considers these methods and their application to the CE-06 data at proton energies of 166, 294, and 330 MeV.

4.4.1 Multiple Scattering Effects

As discussed in App. C, multiple scattering of the recoil ions occurs mainly in the four mylar pressure foils of the CE-06 detector stack. At each foil interface, an ion of nuclear charge Z and energy E effectively scatters into a cone centered about the incident direction, and characterized in angular half-width by $\theta_{\text{rms}} \propto Z/E$. For "typical" ions encountered in this work ($E = 25$ MeV, $Z = 7$), $\theta_{\text{rms}} \approx 0.24°$, so that a scattering of such an ion at the initial pressure foil (see Fig. 3.11) produces an average deflection of 3 mm at the silicon plane.

The primary manifestation of multiple scattering effects in the CE-06 data is a range of ion positions at the silicon array for a particular ion rigidity and PGAC position (the latter measurement is essentially unaffected due the proximity of the foils to the PGAC sense planes). Although, for a given R-x_{pg} pair, a similar effect is produced by motion of the target[18] through the beam, the small spot size ($d_{\text{beam}} < 2$ mm) achieved in the Cooler ring implies a maximum deflection at the silicon of less than 1 mm (i.e., within the

[18] The size of the α calibration source, in fact, produces the finite line width of Fig. 4.8.

detector resolution). For ions with "true" reaction parameters (R, θ_p), the corresponding measurement of this pair by the detector stack yields a range of values in the R-θ_p plane, since the rigidity and projected angle are correlated by the fitting procedures of Sec. C.3.

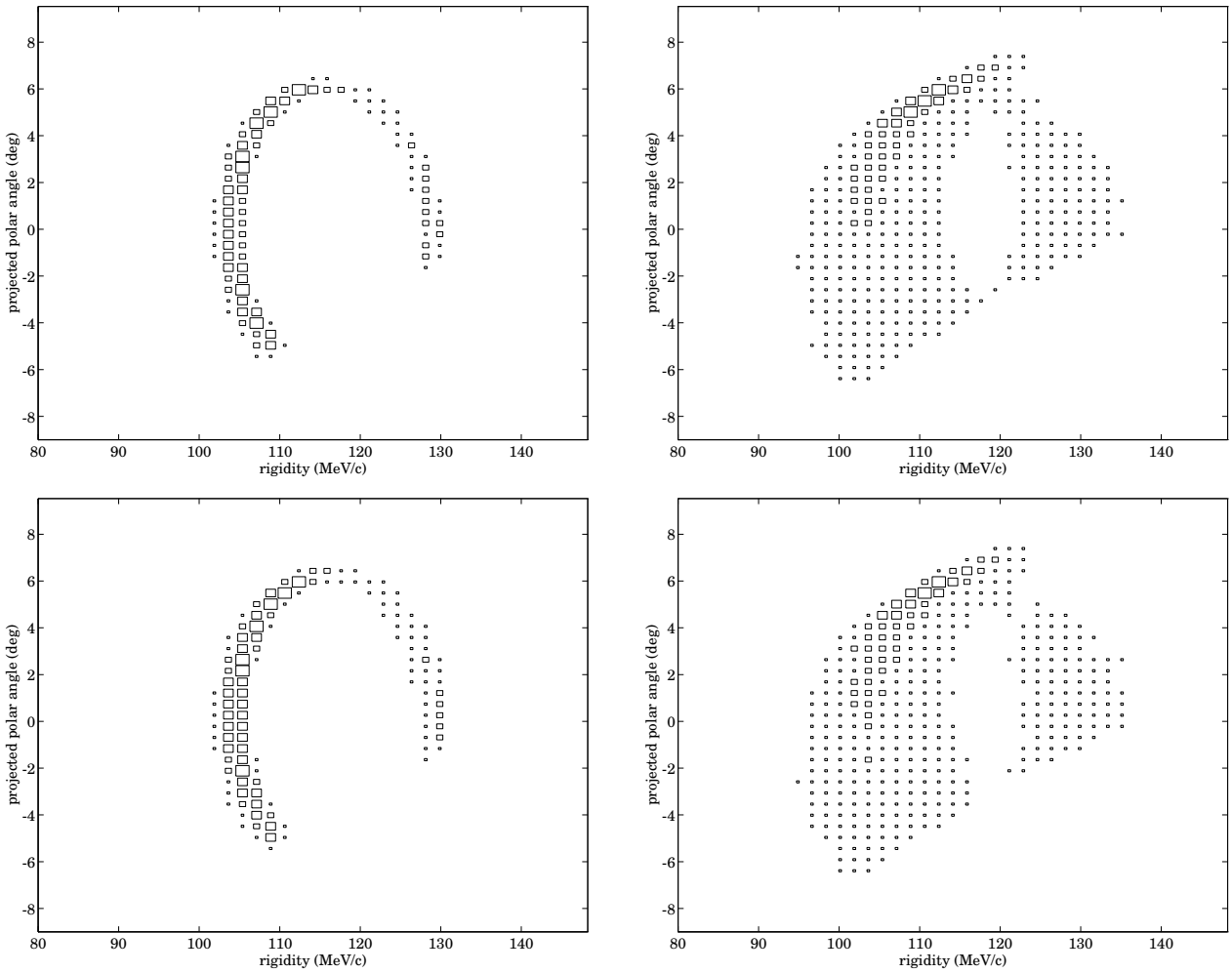

Figure 4.22 Simulation of the measured R-θ_p locus for recoil events corresponding to $^{12}\mathrm{C}(\mathrm{p},\pi^+)^{13}\mathrm{C}^{5+}$ at $E_p = 166$ MeV, using a previously measured [Ho92] pion angular distribution. The bottom (top) row does (does not) include the effects of finite detector resolution, whereas the right (left) column does (does not) include multiple scattering.

Analytical calculations of this effect on the R-θ_p locus are very difficult, if possible at all: the determination of R and θ_p is reasonably complicated (see Eq. (C.2)), and sequential multiple scattering in three foils must be considered (the PC foil is too close to the silicon plane to contribute significantly). Monte Carlo methods based on the forward raytracing of App. C must therefore be used to determine the effects of multiple scattering on the measured angular distributions. Fig. 4.22 shows a simulation of the measurement of the

R-θ_p locus for recoil ions from $^{12}\mathrm{C}(\mathrm{p},\pi^+)^{13}\mathrm{C}^{5+}$ at $E_p = 166$ MeV (compare Fig. 4.18). Not only does the scattering dominate the effects of finite detector resolutions, but also the physical reflection symmetry of the locus about $\theta_p = 0$ is removed.

The concentration of counts near $(R, \theta_p) = (110\ \mathrm{MeV/c}, 5°)$ and dilution of counts close to $(R, \theta_p) = (110\ \mathrm{MeV/c}, -5°)$ suggests that the multiple scattering tends to vary a "true" (R, θ_p) value along a vector with a positive slope of roughly 45° in the figure. In regions where the slope of this error vector and that of the ellipse are similar, the resulting locus is narrow, while a 90° mismatch in slopes causes a maximal broadening of counts. The overall result is that the perceived (measured) distributions can be significantly different from the actual cross-sections. To determine the latter, then, numerical methods directly incorporating the best estimates of multiple scattering effects must be applied.

4.4.2 The Calculation of $d\sigma/d\Omega$

The determination of the differential cross-section in the center-of-mass system, given the true count distribution of events in the lab system, is a fairly straightforward procedure of integration. If $\Delta N_Q(p, \theta, \phi)$ is the number of recoils detected per unit solid angle with charge Q and reaction parameters (p, θ, ϕ), then

$$\Delta N_Q(p, \theta, \phi) = L \cdot T \cdot \left(\frac{d\sigma}{d\Omega}\right)_{\mathrm{lab}} (p, \theta) \cdot P_Q(p) \cdot f_Q(p, \theta, \phi), \tag{4.15}$$

where

$L \equiv$ luminosity averaged over all cycles,

$T \equiv$ total run time (see Table 4.1),

$P_Q(p) \equiv$ probability of charge state Q at ion momentum p, and

$f_Q(p, \theta, \phi) \equiv$ acceptance at (p, θ, ϕ).

The cross-section in the CMS frame, $(d\sigma/d\Omega)_{\mathrm{cms}}$, is then obtained by numerical integration of f_Q in the azimuthal angle ϕ, and application of the Jacobian factor $J(\beta_{\mathrm{cms}}, \theta_{\mathrm{cms}}, \beta)$:

$$\left(\frac{d\sigma}{d\Omega}\right)_{\mathrm{cms}} (\theta_{\mathrm{cms}}) = \frac{\Delta N_Q(p, \theta)}{L \cdot T \cdot J \cdot P_Q(p)} \Big/ \int_0^{\pi} f_Q \, d\phi, \tag{4.16}$$

where β is the ion velocity, and β_{cms} is the CMS velocity in the lab frame. Since the acceptance functions are numerically well-known (see Fig. 4.18), and the other quantities have been previously [Ba81] measured ($P_Q(p)$) or are analytically calculable (J), expressions (4.15) and (4.16) yield the final result of the analysis.[19]

[19] The determination of σ requires knowledge of P_Q, or vice-versa. Using $\sigma(\pi^+)$ from [So81] at 166 MeV, P_Q here agrees within a few percent of previous measurements [Ba81] for typical ion energies.

The results of Sec. 4.4.1, however, demonstrate that the perceived distributions (represented at $E_p = 166$ MeV by Fig. 4.20, for example) can be quite different from $\Delta N_Q(p,\theta)$, the true laboratory angular distribution function, in a manner that is very difficult to calculate analytically. Nonetheless, with the caveat that the simulations of App. C are more heavily relied upon than via Eq. (4.16), the quantity $(d\sigma/d\Omega)_{\rm cms}$ can be calculated numerically, as follows. First, for the reaction process of interest, the measured p-θ spectrum can be generated assuming a "flat" cross-section, $(d\sigma/d\Omega)_{\rm cms} = \sigma_{\rm tot}/4\pi$, resulting in a simulated distribution $n_{\rm sim}(p,\theta)$. The simulated θ vs. p spectrum incorporates the integrated acceptance, detector resolutions, and multiple scattering effects. A comparison of $n_{\rm sim}$ and the measured spectrum for $^{12}{\rm C}({\rm p},\pi^+)^{13}{\rm C}$ at $E_p = 166$ MeV is shown in Fig. 4.23. The lack of counts near $(p,\theta) = (600\ {\rm MeV/c}, 4.5^\circ)$, for example, indicates a significantly smaller CMS cross-section at $\theta_\pi \approx 100^\circ$ (cf. Fig. 4.1) compared to that expected from a flat distribution.

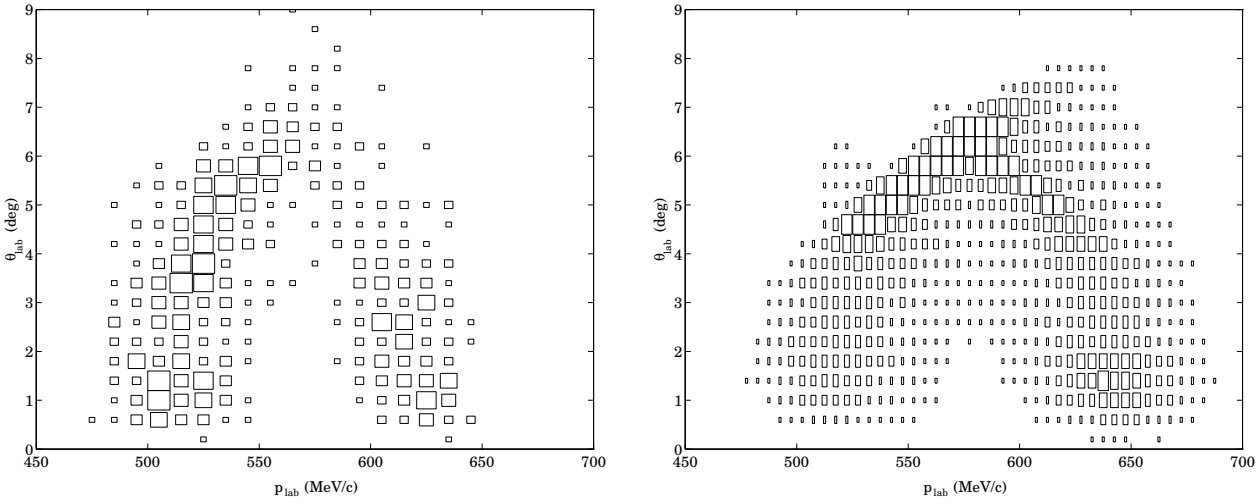

Figure 4.23 Simulated laboratory kinematic spectrum (right) of recoil events corresponding to $^{12}{\rm C}({\rm p},\pi^+)^{13}{\rm C}$ at $E_p = 166$ MeV, for a flat pion distribution in the center-of-mass system. Figure 4.20 is repeated at left for comparison.

Next, weighting factors $w(p,\theta)$ are constructed, as defined by

$$w(p,\theta) \equiv \frac{n_{\rm det}(p,\theta)}{(4\pi/N)\cdot n_{\rm sim}(p,\theta)}, \tag{4.17}$$

where $n_{\rm det}(p,\theta)$ is the number of events in the measured spectrum bin centered at (p,θ), and N is the total number of simulation events thrown. In practice, the simulation counts are more finely binned than the measured p-θ distributions, so that

$$n_{\rm sim}(p,\theta) = \sum_{p_i,\theta_i} n_{\rm sim}(p_i,\theta_i), \tag{4.18}$$

for all simulation bins (p_i, θ_i) contained in the experimental bin centered at (p, θ).

Finally, the differential cross-section in the CMS follows from

$$L \cdot T \cdot \left(\frac{d\sigma}{d\Omega} \right)_{\rm cms} (\theta_{\rm cms}) = w(\theta_{\rm cms}), \tag{4.19}$$

where $\theta_{\rm cms} = \theta_{\rm cms}(p, \theta)$ is given by a Lorentz boost from the laboratory to the CMS system. Statistical uncertainties in the weighting factors are primarily determined by the number of experimental counts per bin (i.e., $n_{\rm det}(p, \theta)$) since, in principle, the total number of simulation events thrown N can be made very large. For this work, N was typically made large enough so that $n_{\rm sim}/n_{\rm det} \gtrsim 100$ for any given region in the p-θ spectrum.[20]

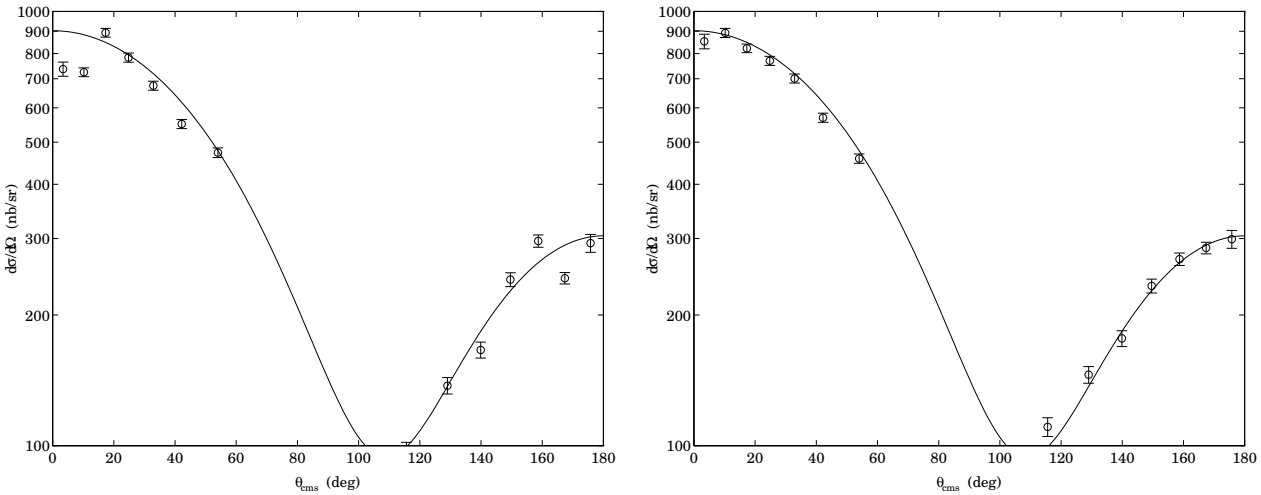

Figure 4.24 Test results of the analysis techniques using (4.17) and (4.19). Both curves are a legendre polynomial fit to ^{12}C(p, π^+)^{13}C data from [Ho92]). Shown is the calculated cross-section assuming no multiple scattering (left), and with multiple scattering (right).

A demonstration of this technique is shown in Fig. 4.24. Here, the expected [Ho92] shape of the summed-state ^{12}C(p, π^+)^{13}C cross-section (for strongly-bound ^{13}C ions) has been used as input to the Monte Carlo simulation programs to create "data," and from this the CMS cross-section has been calculated (or really, regenerated) through Eq. (4.19). The figure shows the results of the cross-section calculation using two simulated count distributions $n_{\rm sim}(p, \theta)$: with and without the inclusion of multiple scattering effects. Although Fig. 4.24 is not a test of the systematic errors involved in this use of the simulations, the distortions produced by the multiple scattering are evidently non-negligible but reasonably well-accounted for by Eq. (4.17). In both graphs of Fig. 4.24, the effects of multiple

[20] This ratio corresponds to a 2% increase in the relative uncertainty of w (compared to $N \to \infty$).

scattering limit the measurement of the cross-section primarily to forward and backward CMS pion angles even at 166 MeV: For $60^\circ \lesssim \theta_\pi \lesssim 110^\circ$, the two branches of the p-θ locus become unresolved. Indeed, the only apparent systematic error occurs at $\theta_\pi \approx 115^\circ$, where the separation of the high-momentum and low-momentum branches is unclear (for example, see the $\theta \approx 5^\circ$ region of Fig. 4.20).

4.4.3 Determination of the Luminosity

The calculation of the integrated luminosity, $L_{\rm int} \equiv L \cdot T$, is an important step in the determination of the absolute cross-sections via Eq. (4.19). Even for the measurement of the π^+/π^0 production ratio R of Eq. (2.1), $L_{\rm int}$ must be fully determined since the CE-06 experiment cannot distinguish ground-state ^{13}C recoils from those in strongly bound excited states. It is conceivable to calculate the $^{12}\mathrm{C}(\mathrm{p},\pi^+)^{13}\mathrm{C}_{\mathrm{g.s.}}$ cross-section from the (summed-state) data by estimation of excited-state population fractions in $^{12}\mathrm{C}(\mathrm{p},\pi^+)^{13}\mathrm{C}$ (using previously measured data [So81]). However, this method to extract the ground-state cross-section is difficult and results in relatively large uncertainties in R (compared to the methods discussed below).

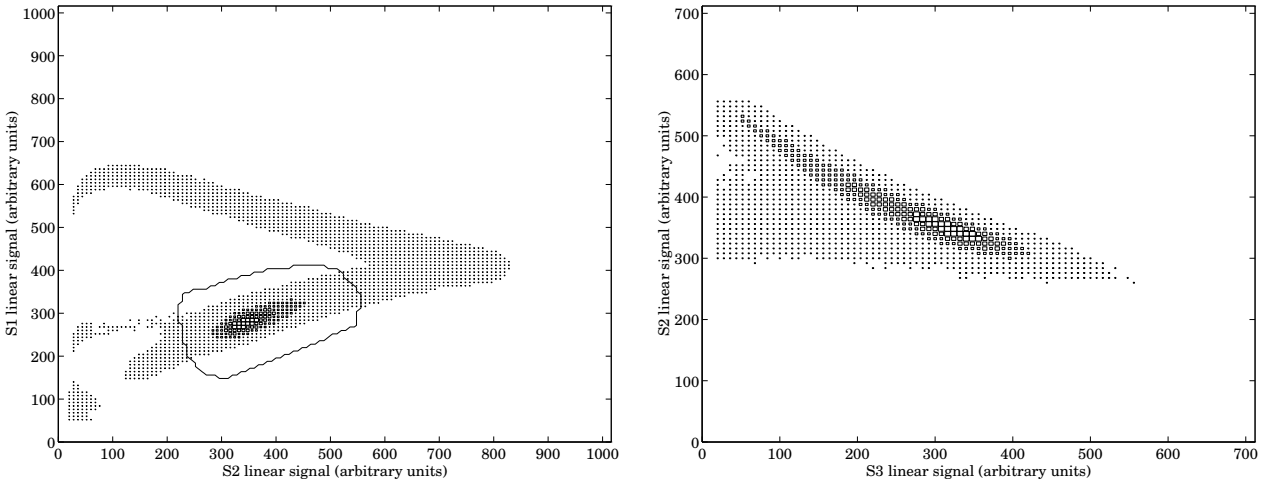

Figure 4.25 Energy loss spectra, taken at $E_p = 330$ MeV, from the monitor scintillators S1, S2, and S3 (see Fig. 3.33). The elastic and inelastic protons are identified as "punch-through" events in S1 vs S2 (left) which are stopped in S3, and which therefore form an $\Delta E \propto 1/E$ locus in S2 vs S3 (right).

As discussed in Sec. 3.4.5, the exclusive concurrent measurement of $^{12}\mathrm{C}(\mathrm{p},\mathrm{p}')^{12}\mathrm{C}^*$ yields in principle an accurate, independent determination of $L_{\rm int}$; however, in practice the detection of low-energy ^{12}C recoils was difficult to achieve. Nonetheless, an attempt was made to use the scintillator portion of the monitor apparatus (see Fig. 3.33) to count

elastically and inelastically scattered protons from the target. Fig. 4.25 shows scintillator data for $E_p = 330$ MeV, where the desired proton counts appear as a strong group in the lower branch of the S1 vs. S2 energy-loss locus. Although the number of protons can reliably be determined, the luminosity calculated [Pp94] from Eq. (3.11) is (at $E_p = 166$ MeV) a factor of roughly 8 greater than that expected from any other rough or careful estimates (see below). The reason for this apparent over-counting, whether due to the difficulty of evaluating the integral of Eq. (3.11) for a rapidly varying cross-section, or because of unexpected and unmeasured small-angle proton background in the ring, remains unclear.

Without a reliable, independent measurement of $L_{\rm int}$, the use of internal data must be resorted to for the determination of absolute cross-sections. Since the CE-06 detector stack is sensitive to all ($Z \geq 4$) ions emitted from the target, there are several possibilities to consider. Perhaps most obvious is the use of ^{12}C ions as a normalization of the luminosity, in analogy to the monitor method described above. Data at $E_p = 166$ MeV clearly indicate (see Fig. 4.14, e.g.) a reasonably strong production of ^{12}C at low energies ($E \lesssim 20$ MeV).

The appearance of these low-energy carbon ions is something of a mystery, however. The kinematics of $^{12}\mathrm{C(p,p')}^{12}\mathrm{C}$ leading to bound ^{12}C states are such that only recoils corresponding to backward proton angles in the CMS ($\theta_p \gtrsim 130^\circ$) are accepted in the lab by the detector stack. Thus, ^{12}C ions corresponding to elastic and inelastic proton scattering from the target enter the silicon array only for $\theta_{\rm lab} \lesssim 25^\circ$, i.e., $E \gtrsim 40$ MeV! Essentially the same kinematics apply[21] to $^{13}\mathrm{C(p,d)}^{12}\mathrm{C}$, for which only ^{12}C ions with $E \gtrsim 50$ MeV are accepted. The large population of low-energy ^{12}C in Fig. 4.14 may be indicative of the possibility that the number of *true* elastic protons in the monitor scintillators have been overcounted; in any case, the internal ^{12}C data cannot be used as a normalization.

Other ions lighter than $M = 12$ appear even more strongly in the CE-06 online data, as in Fig. 4.11. For example, ^{10}B is strongly produced, and the total excitation function of $\mathrm{p} + {}^{12}\mathrm{C} \rightarrow {}^{10}\mathrm{B} + X$ has been measured [Re84], with $\sigma(E) \approx 25$ mb, for $E_p \gtrsim 100$ MeV. The boron angular distributions have not been measured, however, and at least two different reactions can contribute. Furthermore, the unexplained production of ^{12}C may similarly correspond to an anomalous number of ^{10}B events here.

With these considerations, the normalization of the data using ^{13}C recoils from positive

[21] ^{13}C atoms comprise approximately 1% of a natural carbon target.

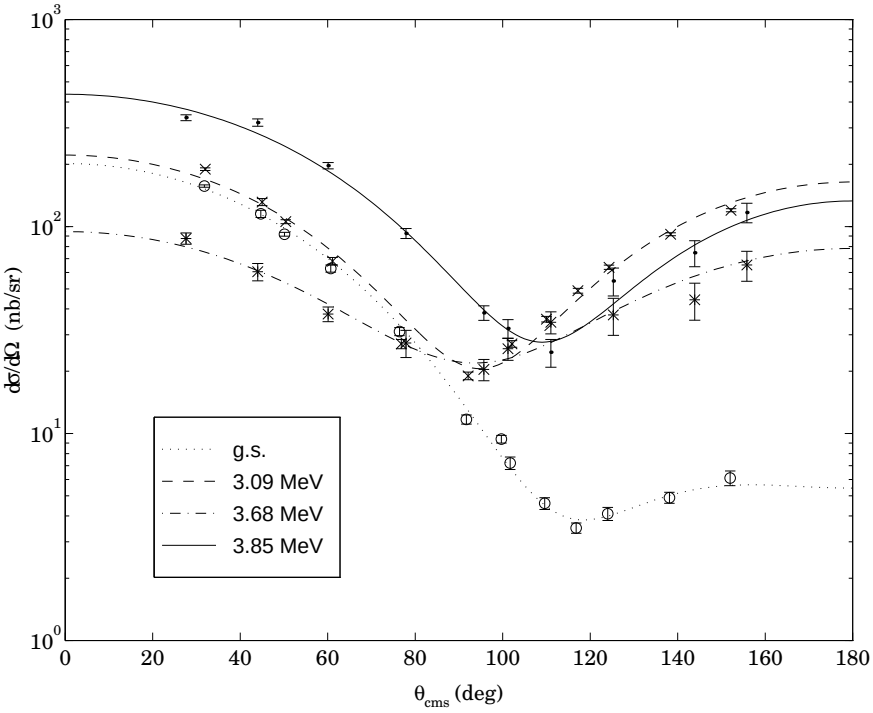

Figure 4.26 Differential cross-sections in the CMS system for $^{12}\mathrm{C}(\mathrm{p},\pi^+)^{13}\mathrm{C}$ leading to the ground state and first three excited states of $^{13}\mathrm{C}$. Data are from [So81]; the solid curves are the result of legendre polynomial fits made here.

pion production is the one remaining feasible candidate in terms of the internal data. Although the total cross-sections are small ($\sigma_{\pi^+} \approx 1\,\mu$b), these recoils are fairly cleanly separated and are produced uniquely via positive pion production. Furthermore, angular distributions for (p,π^+) data have been measured at proton energies nearby to those of interest here. For example, Fig. 4.26 shows data [So81] taken at $E_p = 170$ MeV for $^{12}\mathrm{C}(\mathrm{p},\pi^+)^{13}\mathrm{C}$ leading to the strongly bound states of $^{13}\mathrm{C}$. In order to determine the integrated luminosity, the simulations are used to calculate the acceptance fractions f_i for each of the cross-sections (i = g.s., 3.09 MeV, 3.68 MeV, and 3.85 MeV). Next, an effective cross-section σ_{eff} is constructed: $\sigma_{\mathrm{eff}} = \sum_i f_i\sigma_i$. If N_{exp} is the total number of experimental counts[22] corresponding to $^{12}\mathrm{C}(\mathrm{p},\pi^+)^{13}\mathrm{C}$, then the integrated luminosity is just

$$L_{\mathrm{int}} = \frac{N_{\mathrm{exp}}}{\sigma_{\mathrm{eff}}}. \tag{4.20}$$

The normalization procedure used at 294 MeV and 330 MeV is similar, although angular distributions and total cross-sections are available [Hu87] only at 250 MeV and

[22] Adjusted for the transmission factor (80%) of the detector stack.

354 MeV. To apply the method described by Eq. (4.20), the assumption that the shape of the distribution does not change significantly from proton energies of 354 MeV to 290 MeV was made to determine the acceptance fractions. The value of the total cross-section at $E_p = 294$ MeV was also determined by a smooth interpolation between existing data at 250 MeV, 330 MeV, and 354 MeV.

E_p (MeV)	Runs	$L_{\rm int}$ ($\rm cm^{-2}$)	$L_{\rm data}$ ($\rm cm^{-2}\,sec^{-1}$)	$L_{\rm ave}$ ($\rm cm^{-2}\,sec^{-1}$)
165.4	115–116	$(1.3 \pm 0.2) \times 10^{33}$	$(1.1 \pm 0.1) \times 10^{29}$	$(4.6 \pm 0.5) \times 10^{28}$
293.7	85–104	$(1.5 \pm 0.2) \times 10^{34}$	$(4.2 \pm 0.3) \times 10^{29}$	$(2.7 \pm 0.2) \times 10^{29}$
328.5	106–113	$(1.4 \pm 0.2) \times 10^{34}$	$(6.4 \pm 0.4) \times 10^{29}$	$(4.0 \pm 0.3) \times 10^{29}$

Table 4.3 Results of the luminosity calculations using the internal ^{13}C data corresponding to $^{12}\mathrm{C}(\mathrm{p},\pi^+)^{13}\mathrm{C}$. The $L_{\rm data}$ and $L_{\rm ave}$ columns correspond to $L_{\rm int}$ divided by the last two columns of Table 4.1, respectively.

The final results of this procedure, applied to the February, 1993, CE-06 data at proton energies of 166 MeV, 294 MeV, and 330 MeV are shown in Table 4.3. The luminosities for both the "data-on" and total elapsed times, as calculated using the last two columns of Table 4.1, are also given in the table. The errors given include statistical uncertainties in the CE-06 data and estimated errors in the cross-section normalizations at 294 MeV and 330 MeV.

4.5 Results: 166 MeV, 294 MeV, and 330 MeV

4.5.1 Single-Pion Production at E_p = 166 MeV

Differential cross-section results for positive and neutral pion production at $E_p = 166$ MeV are shown in Figures 4.27 and 4.28, respectively. In both cases, the recoil events have been summed into bins of full-width $\Delta\theta_{\rm lab} = 1.2^\circ$. This size, although much larger than necessitated by the detector stack's intrinsic angular resolution, allows for reasonable statistical uncertainties in the calculated cross-sections. In the case of (p,π^+), the finite width of the low- and high-momentum branches of the recoil locus (as in Fig. 4.20) precludes calculation of the cross-section for $60^\circ \lesssim \theta_\pi \lesssim 110^\circ$ (CMS). For the (p,π^0) measurement, counts were available only for laboratory angles corresponding to forward-scattered pions in the center-of-mass frame.

In general, the agreement of the summed-state $^{12}\mathrm{C}(\mathrm{p},\pi^+)^{13}\mathrm{C}$ measurement here with previous measurements ([Ho92] and [So81]) is good, although the results of this work tend

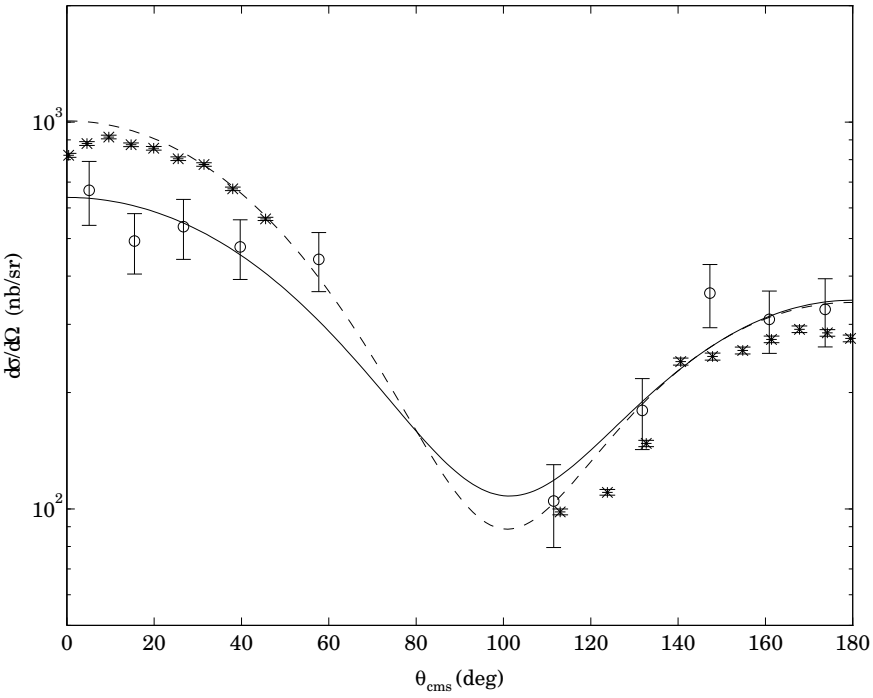

Figure 4.27 Differential cross-section for $^{12}\mathrm{C}(\mathrm{p},\pi^+)^{13}\mathrm{C}$ at $E_p = 166$ MeV, as a function of the pion angle in the CMS. Data from this work are shown by open circles; stars refer to previous recoil data [Ho92]. The dashed line is a sum of (p,π^+) spectrograph data [So81] to separate states in $^{13}\mathrm{C}$. The solid line is a Legendre polynomial fit to the data here.

to underpredict the cross-section at forward angles. Since the small-angle portion of the distribution accounts, in this case, for most of the integrated cross-section, this part of the measurement may be indicative of the systematic error in the calculation using the simulated distributions. For example, when determining the flat simulated distribution at the right of Fig. 4.23, only one kinematical final state could be used without a further assumption upon the relative populations of $^{13}\mathrm{C}$ in the ground state and the three strongly-bound excited states. In particular, the measurement is in best agreement with previous measurements at backward angles, where only the kinematically similar excited states (3.09 MeV $\lesssim E_{\mathrm{ex}} \lesssim$ 3.85 MeV) tend to contribute (as seen in Fig. 4.26).

Only the ground state of $^{13}\mathrm{N}$ is strongly bound, however, and therefore the detection of $^{13}\mathrm{N}$ recoils uniquely corresponds to $^{12}\mathrm{C}(\mathrm{p},\pi^0)^{13}\mathrm{N}_{\mathrm{g.s.}}$. For this measurement, although the effective acceptance was nearly 4π sr, reliable signal events above the background were obtained only for $\theta_\pi \lesssim 45°$. As such, the determination of the total cross-section $\sigma(\pi^0)$ is not possible without making additional assumptions. One possibility is to assume the shape of the cross-section as measured previously [Ho92] and make a fit for the best value

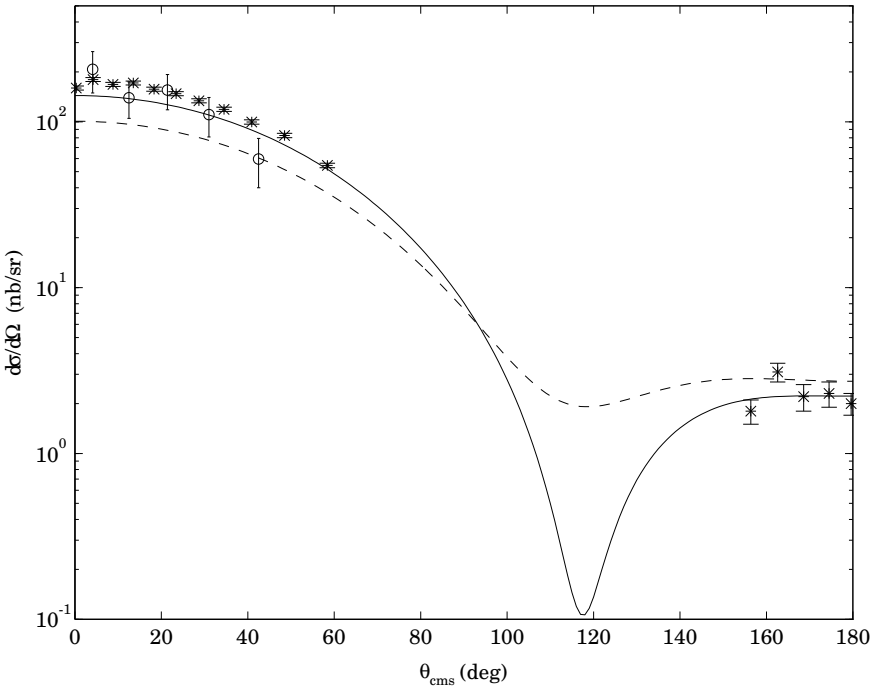

Figure 4.28 Differential cross-section for $^{12}\mathrm{C}(\mathrm{p},\pi^0)^{13}\mathrm{N}_{\mathrm{g.s.}}$ at $E_p = 166$ MeV. Data symbols are the same as in Fig. 4.27. The dashed line is the cross-section [So81] for $^{12}\mathrm{C}(\mathrm{p},\pi^+)^{13}\mathrm{C}_{\mathrm{g.s.}}$, divided by 2. The solid line is a Legendre polynomial fit to the combined (p,π^0) data from [Ho92] and this work.

of the total cross-section. Using the data from this work in Fig. 4.28 and a Legendre polynomial fit to the data of [Ho92], the value $\sigma = 361 \pm 169$ nb is obtained. The relatively large uncertainty in the π^0 data of this work results in a large (50%) error in σ due to the forward-peaked nature of the expected π^0 distribution.

Another method to extract the total cross-section relies on a combination of measured data to allow a reasonable fit to be made. Since the total cross-section is primarily defined by the small-angle portion of the distribution in the (p,π^0) case, the use of external data to constrain the large-angle part of the fit allows a reliable determination of the distribution with a tractable error in the cross-section. Figure 4.28 shows such a fit, using the data of this work ($\theta_\pi < 45°$), and of a previous study [Ho92] for large angles ($\theta_\pi > 150°$), with the final result $\sigma = 374 \pm 46$ nb. This fit is still not constrained enough: the minimum of the distribution close to $\theta_\pi = 120°$ is clearly exaggerated. However, the contribution to the total cross-section from this region ($100° < \theta_\pi < 140°$) is on the order of a few percent (using the expected shape of the distribution from (p,π^+)), i.e., negligible compared to the statistical uncertainty.

Figure 4.28 also shows that the forward-angle portion of the distribution measured

here is in good agreement with that measured before [Ho92], as is the value of the total cross-section ([Ho92] gives $\sigma(\pi^0) = 434 \pm 45$ nb). From the fit to the $^{12}\mathrm{C}(\mathrm{p},\pi^+)^{13}\mathrm{C}_{\mathrm{g.s.}}$ distribution of Fig. 4.26 and the measured $^{12}\mathrm{C}(\mathrm{p},\pi^0)^{13}\mathrm{N}_{\mathrm{g.s.}}$ cross-section here, the ratio of Eq. (2.1) is $R = 1.5 \pm 0.2$. A recent reanalysis [Pi93] of the (p,π^+) data of [So81] and [Gr83] yields a somewhat larger total cross-section for positive pion production, resulting in a ratio here of $R = 1.7 \pm 0.3$. This reanalysis also attempts to calculate Coulomb effects, which tend further to increase the estimate of the strong interaction cross-section, yielding $R = 2.0 \pm 0.3$ using the π^0 result here. It should be noted, however, that this Coulomb calculation results in an anomalous ratio $R = 2.8 \pm 0.4$ when applied to π^+ data at $E_p = 186$ MeV. Whether this discrepancy arises from systematic uncertainty in the π^0 measurement [Ho92] at that energy or from the Coulomb correction of the π^+ cross-section is not clear.

θ_π (deg)	$d\sigma/d\Omega\,(\theta_\pi)$ (nb)
4.1 ± 1.9	207 ± 58
12.5 ± 1.9	139 ± 35
21.4 ± 2.1	155 ± 37
31.0 ± 2.3	111 ± 30
42.5 ± 2.9	60 ± 20

$\sigma(\pi^+)$ (nb)	$\sigma(\pi^0)$ (nb)	R
555 ± 5 [Gr83]	374 ± 46	$1.5 \pm .2$
635 ± 76 [Pi93]	374 ± 46	$1.7 \pm .3$
750 ± 90 [Pi93]	374 ± 46	$2.0 \pm .3$

Table 4.4 Results of the analysis at 166 MeV. Differential cross-sections for $^{12}\mathrm{C}(\mathrm{p},\pi^0)^{13}\mathrm{N}_{\mathrm{g.s.}}$ (left) are given in the center-of-mass frame. The uncertainties listed in the first row of the ratio table (right) are statistical only.

The (p,π^+) cross-section results and ratio calculations are summarized in Table 4.4. Although the absolute measurement of $\sigma(\pi^0)$ here in fact depends on the corresponding value of the $^{12}\mathrm{C}(\mathrm{p},\pi^+)^{13}\mathrm{C}_{\mathrm{g.s.}}$ cross-section, this dependence is very weak (and much smaller than the listed statistical error in $\sigma(\pi^0)$) since the integrated bound-state cross-section is primarily populated by the first three ^{13}C excited states. Furthermore, no Coulomb analysis has yet been made for the excited-state cross-sections, hence Table 4.4 lists only the final result $\sigma(\pi^0) = 374 \pm 46$ nb.

4.5.2 Single-Pion Production at 294 and 330 MeV

Figure 4.29 shows the results of this work for positive-pion production at proton energies of 294 and 330 MeV. The measurements as shown are limited to pion emission angles in the CMS of $\theta_\pi \lesssim 30°$, due to the finite acceptance of the detector stack at

these energies (see Fig. 4.19). For $E_p \approx 300$ MeV, the silicon array admits ^{13}C recoils corresponding to CMS pion angles of $\theta_\pi \lesssim 45°$ and $\theta_\pi \gtrsim 120°$; however, no ^{13}C events in the high-momentum branch (above background) were seen at either 294 or 330 MeV. This result suggests that the differential cross-section for (p, π^+) leading to bound ^{13}C states is less than roughly 10 nb for backward scattered pions ($\theta_\pi \gtrsim 120°$). Furthermore, in contrast to the results at $E_p = 166$ MeV, no backward peak in the distribution is manifested: simulations show that, given a flat CMS distribution, approximately 50% of the total detected ^{13}C events would correspond to $\theta_\pi > 140°$. The results here at proton energies of 294 MeV and 330 MeV limit any backward peak to less than 1% of the differential cross-section at $\theta_\pi = 0°$ (for $E_p = 166$ MeV, $\sigma(0°)/\sigma(180°) \approx 50\%$).

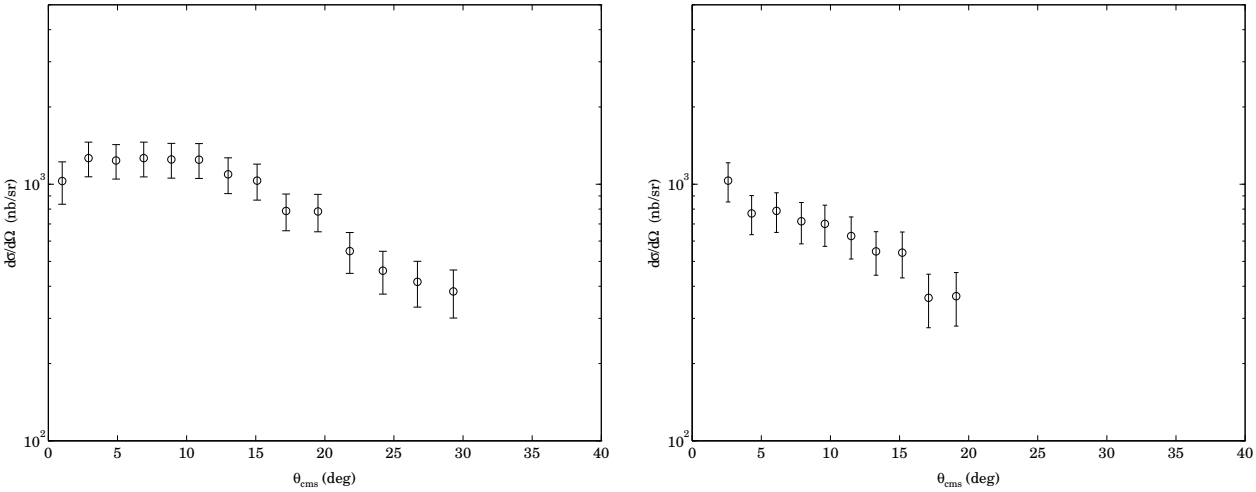

Figure 4.29 Differential cross-section $d\sigma/d\Omega$ for $^{12}\mathrm{C}(\mathrm{p}, \pi^+)^{13}\mathrm{C}^*$ as a function of the pion angle in the center-of-mass frame. Shown are the summed-state results at $E_p = 293.7$ MeV (left) and $E_p = 328.5$ MeV (right).

The cross-sections reported here for production of positive pions, along with previous measurements [Hu87] of $^{12}\mathrm{C}(\mathrm{p}, \pi^+)^{13}\mathrm{C}^*$, are shown in Fig. 4.30, plotted as a function of the Mandelstam variable t, the square of the four-momentum transfer.[23] For the data measured here, the forward-angle cross-section is essentially independent of s (the square of the total four-momentum), holding t constant. This feature has also been seen [Hu87] for $E_p > 350$ MeV and $t = 0.5$ GeV^2/c^2 in the ground state and 9.5 MeV excited state of ^{13}C (the latter is unbound and not detected in this work). However, the small absolute value of the cross-sections measured here, compared to a smooth extrapolation to

[23] The larger values of t in Fig. 4.30 correspond to smaller pion scattering angles.

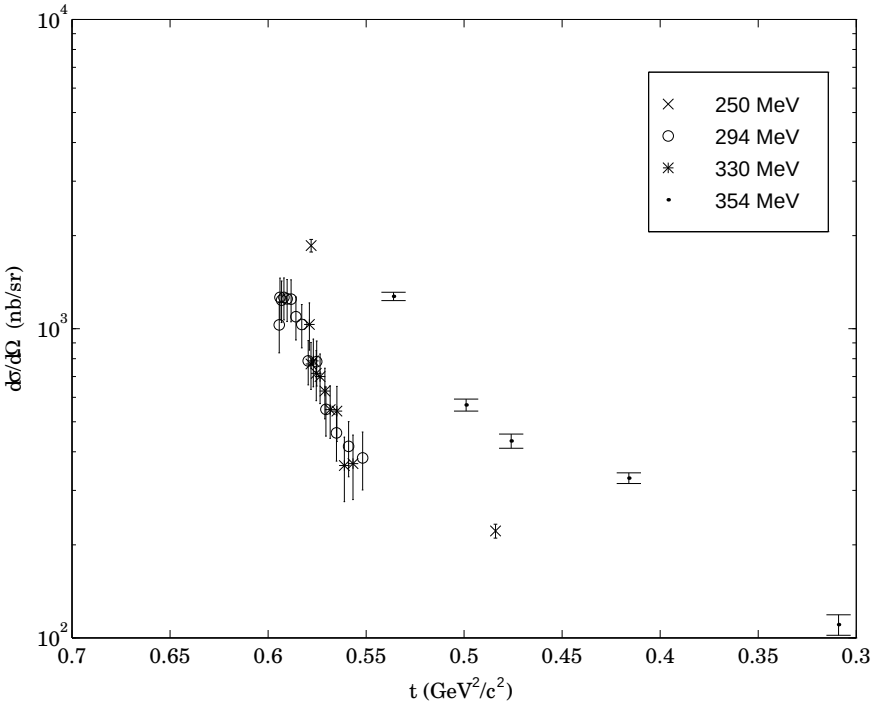

Figure 4.30 Differential cross-sections for positive pion production at intermediate energies, leading to the strongly-bound states of ^{13}C, as a function of the four-momentum transfer. Data at 250 and 354 MeV are from [Hu87].

$t > 0.55$ GeV^2/c^2 of the data at 250 and 354 MeV, is unexpected, and most likely is the result of the systematic errors involved in the calculation of the absolute luminosity at 294 and 330 MeV. In this regard, the absolute scaling of the cross-sections at these energies in Fig. 4.30 should be considered preliminary.

Figure 4.31 shows the results of the analysis for ^{12}C(p, π^0)^{13}N at $E_p = 294$ MeV. Construction of the lower edge of the $Z = 7$ gate applied to the particle ID (see Fig. 4.12) is especially difficult in this situation, given the expected small number of nitrogen events compared to the relatively strong carbon locus. Background ^{12}C events which "leak" into the nitrogen gate tend to appear in the mass-13 and mass-14 region of the calculated mass array. The energy signature of nitrogen events compared to that for carbon recoils is well separated for the low-momentum branch of the (p, π^+) loci (see Table C.1); nonetheless, a clear ^{13}N M-Q locus was not obtainable, as seen in the left graph of Fig. 4.31. The corresponding cross-section results, for a total of approximately 80 ^{13}N events, are preliminary.

For the integrated luminosity given in Table 4.3 at 294 MeV, roughly 2000 ^{13}C events corresponding to ^{12}C(p, π^+)^{13}C were recorded. Although the population of ^{13}N

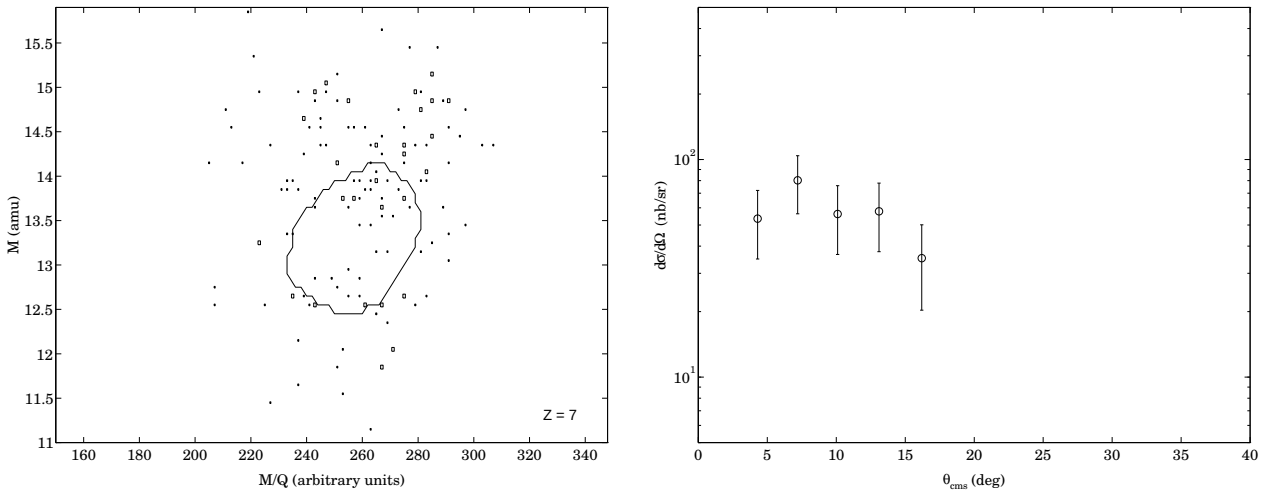

Figure 4.31 Preliminary cross-sections for $^{12}\mathrm{C}(\mathrm{p},\pi^0)^{13}\mathrm{N}$ at 294 MeV. The differential cross-section (right) is derived from events satisfying the M and M/Q gate shown at left (compare Fig. 4.16).

via $^{12}\mathrm{C}(\mathrm{p},\pi^0)^{13}\mathrm{N}_{\mathrm{g.s.}}$ should be only a factor of two smaller than the number of ^{13}C events from $^{12}\mathrm{C}(\mathrm{p},\pi^+)^{13}\mathrm{C}_{\mathrm{g.s.}}$, the strongly-bound excited states of ^{13}C (which together with the ground state produce Fig. 4.29) are strongly populated via (p,π^+). At $E_p = 354$ MeV, the ground state contribution is approximately 15% [Hu87] of the total bound-state ^{13}C production; a similar ratio exists at $E_p = 166$ MeV (see Fig. 4.26). Taking this relative weakness of the ground state into account, a better estimate of the number of ^{13}N events detected is $N_{\pi^0}(294\ \mathrm{MeV}) \approx 100$, assuming a forward-peaked CMS angular distribution.

The total number of ^{13}N events is therefore in reasonable agreement with that expected ($N \approx 100 \pm 15$) from the number of ^{13}C events corresponding to (p,π^+). More precisely, if R is the ratio $\sigma(\pi^+)/\sigma(\pi^0)$ for production of the ground states of ^{13}C and ^{13}N (see Eq. (2.1)) at $E_p = 294$ MeV, then the expected number of ^{13}N events from (p,π^0) is

$$N_{\pi^0}\,(294\,\mathrm{MeV}) \approx \frac{200 \pm 30}{R}. \tag{4.21}$$

Here, the numerator in Eq. (4.21) is derived from the total number of π^+ events obtained, the expected population fraction of $^{13}\mathrm{C}_{\mathrm{g.s.}}$ compared to all bound states, and acceptance fraction of π^0 events compared to π^+ events. This calculation is independent of the absolute luminosity, and shows that the number of π^0 events at 294 MeV (≈ 80) is consistent with a ratio in the range $R \approx 2.2$–2.8. This figure is somewhat higher than that expected from isospin invariance; however, the relatively large error in this measurement of R renders any such conclusions premature.

4.5.3 Double-Pion Production at E_p = 330 MeV

Given the large $Z = 5$ background and limited number of reliable ^{13}N candidates, evidence for $(\mathrm{p}, \pi\pi)$ events is most likely to be found via detection of ^{13}C recoils corresponding to $^{12}\mathrm{C}(\mathrm{p}, \pi^+\pi^0)^{13}\mathrm{C}$. Fig. 4.32 shows data from the 294 MeV and 330 MeV runs for recoils with[24] $Z = 6$, $Q = 5$, and $M = 13$ that satisfy broad conditions in silicon energy and time-of-flight, according to the kinematics of $(\mathrm{p}, \pi\pi)$ shown in Fig. 2.8. In principle, *any* ^{13}C recoil events in the $\pi\pi$ kinematic region of the R-θ_p plane (bounded by the solid lines of Fig. 4.32) uniquely identify $^{12}\mathrm{C}(\mathrm{p}, \pi^+\pi^0)^{13}\mathrm{C}^{5+}$ events.

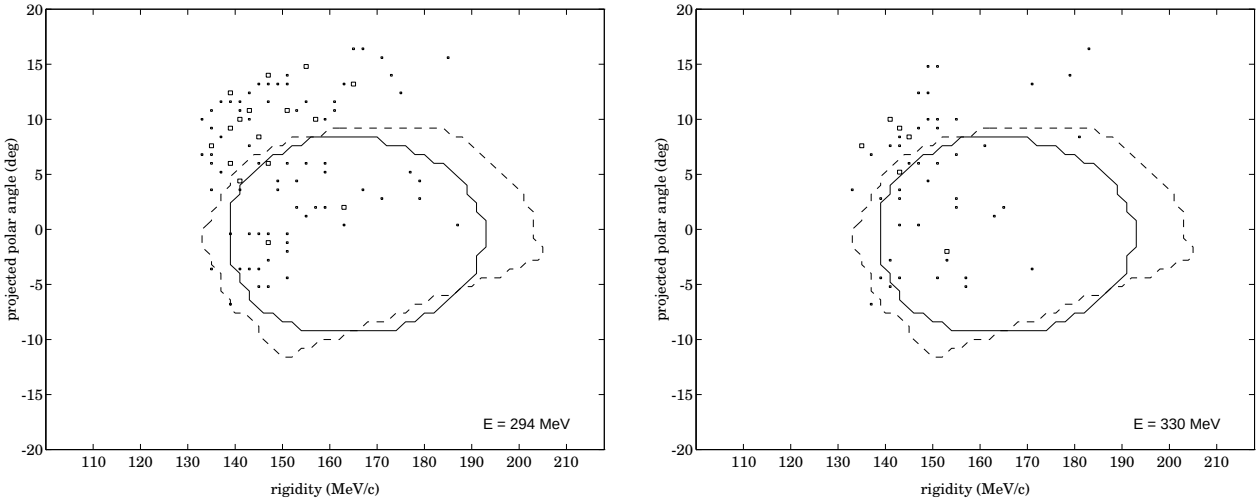

Figure 4.32 Results of the search for ^{13}C events from $(\mathrm{p}, \pi\pi)$ production, for recoils satisfying $Q = 5$, $M = 13$, and $Z = 6$ gates. The solid line denotes the possible kinematic region in the R-θ_p plane for recoils from $^{12}\mathrm{C}(\mathrm{p}, \pi^+\pi^0)^{13}\mathrm{C}$; the dashed line extends this region to account for multiple scattering and finite detector resolutions.

Given a total cross-section for $(\mathrm{p}, \pi^+\pi^0)$ on the order of $\sigma_{\pi\pi} \approx 10$ nb, the expected number of $^{13}\mathrm{C}^{5+}$ recoils detected is on the order of 10, for the 330 MeV runs analyzed here. At $E_p = 294$ MeV, just below the threshold for $^{12}\mathrm{C}(\mathrm{p}, \pi^+\pi^0)^{13}\mathrm{C}_{\mathrm{g.s.}}$ of $E_p = 297$ MeV, the 39 ± 7 counts in the dashed area of Fig. 4.32 (calculated from kinematics and simulations incorporating multiple scattering and detector resolutions) represent the background for this measurement. Assuming that this background strength remains constant from 294 to 330 MeV, an enhanced count rate at 330 MeV would be direct evidence for $(\mathrm{p}, \pi\pi)$ events.

However, after scaling the 330 MeV data by the ratio $L_{\mathrm{int}}(294\ \mathrm{MeV})/L_{\mathrm{int}}(330\ \mathrm{MeV})$, the number of $\pi\pi$ candidate events in the dashed region in the right graph of Fig. 4.32

[24] The background level was smaller for $Q = 5$ than for the other charge states.

is 29 ± 7. Thus, the $\pi\pi$ signal strength is statistically the same as the background level, and no measurement of the cross-section can be made here. Nonetheless, an upper limit on the total cross-section for $^{12}\mathrm{C}(\mathrm{p},\pi^+\pi^0)^{13}\mathrm{C}$ at $E_p = 330$ MeV can be calculated. With $N_{\pi\pi} \approx N_{\mathrm{bkgd}} \approx 39$, the expected mean number of $\pi\pi$ events is $\mu = 0 \pm \sqrt{39} = 0 \pm 6.3$, with a 95% confidence limit of $N_{\pi\pi} < 13$. Using the calculated acceptance for $^{13}\mathrm{C}$ recoils from $^{12}\mathrm{C}(\mathrm{p},\pi^+\pi^0)^{13}\mathrm{C}^{5+}$, and the integrated luminosity $L_{\mathrm{int}}(330\ \mathrm{MeV}) = 14.2\ \mathrm{nb}^{-1}$, the upper limit is $\sigma_{\pi\pi} < 17$ nb, at the 95% confidence level. As a fraction of the total cross-section for (p,π^+) leading to bound $^{13}\mathrm{C}$ states at 330 MeV, this limit corresponds to $\sigma(\pi^+\pi^0)/\sigma(\pi^+) < 0.009$.